



1 Mechanical compaction mechanisms in the input sediments of the  
2 Sumatra Subduction Complex- insights from microstructural analysis of  
3 cores from IODP Expedition- 362

4 Sivaji Lahiri<sup>1\*</sup>, Kitty L. Milliken<sup>2</sup>, Peter Vrolijk<sup>3</sup>, Guillaume Desbois<sup>1</sup>, Janos L. Urai<sup>1</sup>

5 <sup>1</sup>Institute of Tectonics and Geodynamics, RWTH Aachen University, Germany, Lochnerstrasse 4–20, 52056,  
6 Aachen, Germany

7 <sup>2</sup>Bureau of Economic Geology, The University of Texas at Austin, Austin, TX, 10611, USA

8 <sup>3</sup>Applied Ocean Science and Engineering, Woods Hole Oceanographic Institution, Woods Hole, MA, United  
9 States

10 \* Corresponding author: [sivaji.lahiri2@gmail.com](mailto:sivaji.lahiri2@gmail.com)

11

12 Abstract

13 The input sediments of the North Sumatra subduction zone margin, drilled during IODP Expedition 362, exhibit  
14 remarkable uniformity in composition and grain size over the entire thickness of the rapidly deposited Nicobar  
15 Fan succession (sea-floor to 1500 mbsf depth), providing a unique opportunity to study the micromechanisms of  
16 compaction. Samples were prepared from dried core samples from sites (U1480 and U1481) by both Ar-ion cross-  
17 section polishing and broad-ion beam cutting, and imaged with a field-emission SEM. Shallowest samples (sea-  
18 floor to 28mbsf) display a sharp reduction in porosity from 80% to 52% due to collapse of large clay-  
19 domain/matrix pores associated with rotation and realignment of clay-platelets parallel to the bedding plane. The  
20 deeper succession (28mbsf to 1500mbsf) exhibits less rapid reduction in porosity from 52% to 30% by the  
21 progressive collapse of silt-adjacent larger pores by bending and subsequent sliding/fracturing of clay particles. In  
22 addition, there is a correlated loss of porosity in the pores too small to be resolved by SEM.

23 Clastic particles show no evidence of deformation or fracturing with increasing compaction. In the phyllosilicates,  
24 there is no evidence for pressure solution or recrystallization: thus, compaction proceeds by micromechanical  
25 processes. Increase in effective stress up to 18 MPa (~1500mbsf) causes the development of a weakly aligned  
26 phyllosilicate fabric defined by illite clay particles and mica grains, while the roundness of interparticle pores  
27 decreases as the pores become more elongated. We propose that bending of the phyllosilicates by intracrystalline  
28 slip may be the rate-controlling mechanism.

29 Pore size distributions show that all pores within the compactional force chain deform, irrespective of size, with  
30 increasing compactional strain. This arises because the force chain driving pore collapse is localized primarily



31 within the volumetrically dominant and weaker clay-rich domains; pores associated with packing around isolated  
32 silt particles enter into the force chain asynchronously and do not contribute preferentially to pore loss over the  
33 depth range studied.

## 34 Introduction

35 Muds are fine-grained sediments (>50% of particles <63µm diameter) comprising platy detrital clay minerals and  
36 equidimensional detrital grains such as quartz, feldspar, calcite, etc. (Nakano, 1967; Hesse, R., 1975; Sintubin,  
37 1994). Understanding the mechanical, chemical, and microstructural properties of mud and mudstone is of great  
38 interest for rock property prediction in basic earth science, in exploration, subsurface integrity studies and  
39 geotechnical engineering (Yagiz, S., 2001; Aplin and Yagiz, 2011; Lazar et al., 2015). The chemical and physical  
40 behavior of marine muds plays a critical role in defining the geometry of accretionary prisms, locating the  
41 décollement for fault rupture (Vrolijk, 1990; Chester et al., 2013) and understanding subduction zone earthquakes  
42 and tsunamis (Dean et al., 2010; Chester et al., 2013; Hüpers et al., 2017).

43 Marine mud is deposited with a highly porous isotropic fabric (Bowles, 1969; Bennett et al. 1981; Bennett et al.  
44 1991); depositional porosity in mud is about twice as high as in sand (e.g., Velde, 1996, Lundegard, 1992). In  
45 contrast, mudstones have low porosities, modal pore sizes measured in nm, and an absence of textural controls on  
46 porosity (e.g. Aplin et al., 2006; Milliken et al., 2012; Milliken et al., 2013). The processes in this dramatic  
47 evolution of porosity has similarities to compaction of sand to sandstone, comprising a combination of compaction  
48 and cementation (Milliken and Day-Stirrat, 2013), although the much smaller, elongated phyllosilicate grains  
49 increase the role of clay-bound water in the process (Karaborni et al., 1996). Whereas a refined and somewhat  
50 predictive understanding exists for porosity evolution in sand and sandstones (e.g., Lander and Walderhaug, 1999;  
51 Paxton et al., 2002; Lander et al., 2008; Adjukiewicz and Lander, 2010, Desbois et al., 2011), such a model is at  
52 best preliminary for muds and mudstones (Pommer and Milliken, 2015; Milliken and Olson, 2017). It seems clear  
53 that the composition of the grain assemblage importantly sets the stage for porosity evolution in muds (Milliken,  
54 2014), cementation being the greatest in muds with abundant biogenic debris. In contrast to sandstones, however,  
55 cementation is far less common globally in mudstones (Milliken, 2019), leading to the notion that mechanical  
56 compaction may be far more important in muds. Establishing the expected compaction behavior for muds in a  
57 setting of well-constrained mud properties is an essential contribution that our study hopes to serve.

58 Investigations of mud and mudstone compaction are usually based on proxy data, such as velocity or density,  
59 rather than direct measurements of porosity (e.g., references in Mondol, 2007). Direct measurement of porosity  
60 can be broadly classified into two categories: 1) laboratory experiments; (e.g., Mitchell, 1956; Bennett et al. 1981;  
61 Vasseur et al. 1995; Mondol et al. 2007; Fawad et al. 2010; Emmanel and Day-Stirrat, 2012), and 2) studies on  
62 natural samples (e.g., Meade, 1964; Ho et al., 1999; Aplin et al. 2003, 2006; Day-Stirrat et al., 2008; 2010; 2012;  
63 Milliken et al, 2012, Milliken et al., 2013). A common shortcoming of studies on natural samples is the assumption  
64 that the bulk porosity is a direct measure of compaction although porosity loss has contributions of both  
65 compaction and cementation (Lundegard, 1992; Ehrenberg, 1989; Paxton et al., 2002), and this can only be  
66 accomplished by petrographic inspection (Milliken and Curtis, 2017). Experimental studies generally avoid this  
67 shortcoming by the use of lab-produced particle packs that undergo no chemical change during the experiment.



68 Studies of shallowly buried units (like the present study) are the ones most likely to avoid the complication of  
69 cementation, especially if temperatures are low and bulk grain assemblages are siliciclastic (Milliken, 2014).

70 Previous studies report contrasting ideas about the mechanisms of mechanical compaction of mud. According to  
71 some studies, burial compaction significantly increases the alignment of phyllosilicate (clay and mica) parallel to  
72 the bedding planes (Bowles et al., 1969; Oertel and Curtis, 1972; Vasseur et al., 1995). Other studies state that  
73 intense mechanical compaction has a limited impact on the development of phyllosilicate fabric in mud (Ho et al.,  
74 1999; Aplin et al., 2006; Day-Stirrat et al., 2008; 2011). These studies investigated the changes in particle  
75 alignment and reduction in porosity (Ho et al., 1999; Aplin et al., 2006; Day-Stirrat et al., 2008; 2011) but without  
76 imaging the evolution of pore morphology with increasing compactional strain. This is where this study aims  
77 contribute.

78 We received 55 mud samples from drill cores collected during IODP Expedition 362 west of the North Sumatra  
79 subduction zone margin and investigated the evolution of petrographic microstructure and pore morphology as a  
80 function of compactional strain. Apart from general implications for global mudrocks, we hope this investigation  
81 will also contribute to studies that seek to predict rock properties in the deeper subsurface at the Sumatra  
82 subduction front.

83

## 84 Geological background and drilling

85 The Sumatra subduction zone extends 5000km from the Andaman-Nicobar Islands in the northwest to the Java-  
86 Banda arc in the Southeast (Fig.1a and b) (Prawirodirdjo et al., 1997; Hippchen and Hyndman, 2008). The trench  
87 of the Sumatra subduction zone (Fig.1a) developed on the subducting Indo-Australian Plate at a convergence rate  
88 of 5.5 cm/yr in the north and 7.23 cm/yr in the South (Ghosal et al., 2014; Moeremans, and Singh, 2015).

89 On 26th December 2004, the west coast of Northern Sumatra recorded one of the largest earthquakes (Mw-9.3) in  
90 the 21st century, generating a devastating Tsunami in the Indian Ocean (Ammon et al., 2005; Lay et al., 2005).  
91 Understanding the mechanism(s) behind this unprecedented event was the central idea behind IODP Expedition  
92 362. The main objective of the expedition was to collect core and log data of the incoming sedimentary succession  
93 of the Indo-Australian oceanic plate to understand the seismogenic process related to the margin (Dugan et al.,  
94 2017; McNeill et al., 2017). During the expedition in 2016, drilling was performed on two sites (U1480 and U1481)  
95 located on the oceanic plate west of the North Sumatra subduction margin and east of the Ninety East Ridge  
96 (Fig.1a, b) (Dugan et al., 2017). The drilling sites recovered a complete, 1.5 km thick sedimentary section from  
97 late Cretaceous to Pleistocene down to the basement of basaltic crust (Dugan et al., 2017; McNeill et al., 2017).

98 The input sedimentary section of the Sumatra subduction zone comprises the distal part of the trench wedge,  
99 Nicobar fan sequence, and pre-fan pelagic section on the basaltic crust at the bottom (Dugan et al., 2017; McNeill  
100 et al., 2017). At Site U1480, the entire recovered section was categorized into six lithological entities, Units I to  
101 VI (Fig. 1c) (McNeill et al., 2017). Unit I (0 to 26.72 mbsf) consists of unconsolidated calcareous clay, silty clay



102 with alternating fine sand (McNeill et al., 2017). Unit II from 26.72 to 1250 mbsf consists of alternating fine-  
103 grained sand and silty clay to silt (McNeill et al., 2017). Unit III (1250 ~ 1327 mbsf) is divided into two subunits:  
104 Unit IIIA and IIIB (McNeill et al., 2017). Unit IIIA consist of thin to medium-bedded, gray-green or brown  
105 mudstone and intercalated siltstone, and Unit IIIB is composed of reddish-brown tuffaceous silty claystone with  
106 fragmented sponge spicules and radiolaria (McNeill et al., 2017). The boundary between Units IIIA and IIIB (1310  
107 mbsf) at this site marks the base of the Nicobar Fan and the beginning of the thin pre-fan succession (Pickering et  
108 al., 2020). Units IV, V, and VI include volcanoclastic rocks with tuffaceous sandstone, conglomerates, and basaltic  
109 oceanic crust, respectively. For this study, we restricted ourselves to the Nicobar fan sequence that comprises Unit  
110 I, II, and IIIA. At Site U1481, the pre-fan succession was not encountered and a Unit III, a thicker equivalent of  
111 Subunit IIIA at Site U1480, represents the material of the lower Nicobar Fan (see Figure F15, in Site U1481 report;  
112 McNeil et al., 2017).

113 X-ray diffraction (XRD) and bulk rock analysis at Site U1480 (in Units I and II) show a clay mineral assemblage  
114 dominated by illite, with minor smectite and chlorite (Supplementary data-1) (Rosenberger et al., 2020). The  
115 smectite content decreases with depth with the mean value of 33 wt% in Unit I and 17 wt% in Unit II (Table 1)  
116 (Rosenberger et al., 2020). However, the relative abundance of smectite content increases sharply in Unit IIIA  
117 with a mean value of 73 wt%. The illite percentage in the clay assemblage increases down section from Unit I to  
118 Unit II from a mean of 49 wt% to 59 wt%; whereas decreases in Unit IIIA with a mean of 19 wt%. The  
119 expandability of the illite/smectite mixed-layer increases down-section, which signifies an opposite trend to the  
120 one expected for burial diagenesis (Rosenberger et al., 2020). Clay mineralogy in the lower fan muds of Unit III  
121 of Site U1481A contains an average of 37 percent smectite and 37 percent illite (Rosenberger et al., 2020).

122 The Nicobar fan sequence exhibits almost compositionally homogeneous (silt/clay ratio; mostly 'silty-clay')  
123 subunits with uniform grain size (McNeill et al., 2017), and also a history of rapid deposition (125-290 m/my;  
124 Backman et al., 2019). The drilling sites are 255 km away from the deformation front, thus the samples are  
125 undisturbed by tectonic faulting. In addition, the scarcity of biogenic grains and low temperatures (<68°C) make  
126 cementation only as highly localized concretions (McNeil et al., 2017; Torres and Milliken, 2019). Such a  
127 homogeneous sedimentary secession extending across 1.5 km depth is rare in sedimentary basins. Hence, these  
128 samples provide us with a unique opportunity to study depth-wise variation in microstructure as a function of  
129 vertical effective stress with few complications from multiple causes of porosity loss.

## 130 Sampling and Methods

131 This study is based on two sample sets that were obtained from Sites 1480 (Holes E, F, G, and H) and 1481 (Hole  
132 A) independently, and analyzed by slightly different methods. The first sample set (33 mud samples; depth 1.24  
133 to 1300 mbsf) was prepared and analyzed using BIB-SEM at RWTH Aachen University, Germany. The second  
134 sample set (22 samples; depths 6.25 to 1493.30 mbsf) was prepared using Ar-ion cross-section polishing and  
135 imaged by field-emission SEM at the Bureau of Economic Geology (BEG) at the University of Texas at Austin.  
136 Core description of the analysed 55 mud samples are tabulated in Supplementary data-2.



137 [BIB-SEM technique \(analysis of the first set of samples, Aachen University\)](#)

138 [Sample preparation for BIB-SEM and imaging](#)

139 We received 33 freeze-dried mud samples from the IODP repository, Japan (SN-1 to SN-33 in Table-1). The  
140 samples were collected using a tube inserted perpendicular to the cut face of the drill core in such a way that the  
141 notch of the tube identified the top of the sample so the orientation of bedding planes for each sample was known.  
142 In Fig. 1d, a tube sample received from the IODP repository is shown, where the red line on the top of the tube  
143 identifies the notch. Subsamples ( $10 \times 5 \times 2 \text{ mm}^3$ ) were cut from the individual freeze-dried samples using a razor  
144 blade. These subsamples were pre-polished using silicon carbide (SiC) paper to reduce the roughness of the surface  
145 down to  $10 \mu\text{m}$ . Further, Broad Ion Beam (BIB) polishing was carried out using a JEOL SM-09010 cross-section  
146 polisher for 10 hours at 6 kV and  $150 \mu\text{A}$ . BIB reduces surface damage by removing a  $100 \mu\text{m}$  thick layer to  
147 generate a high-quality polished cross-section of  $1\text{-}2 \text{ mm}^2$  with a topography less than  $5 \text{ nm}$  (Desbois et al., 2009).

148 After polishing, the BIB cross-sections were coated with tungsten and imaged with a Zeiss Supra 55 SEM with  
149 SE2, BSE, and EDX detector (Supplementary data-3). SE2 images were used to image porosity, while for  
150 identifying phases BSE images are combined with an EDX map as well as EDX point analysis. For each cross-  
151 section, we made mosaics of hundreds of SE2 and BSE images at a magnification of  $20,000\times$  ( $\sim 14.3 \text{ nm}$  pixel  
152 value) and  $10,000\times$  respectively, with an overlap of 20% to 30%, (Klaver et al., 2012; 2015; 2016; Hemes et al.,  
153 2013; 2015; 2016; Laurich et al., 2014). The mosaics are stitched together using Aztec software preserving the  
154 original pixel resolution. Finally, these stitched images are used for the segmentation of pore spaces, minerals, and  
155 other respective analyses.

156 [Image segmentation and pore analysis](#)

157 For quantifying porosity and pore morphology, individual SE2 image mosaics were segmented using a ‘seed and  
158 grow’ algorithm (Adams and Bischof (1994)) implemented with a MatLab code (Jiang et al., 2015; Schmatz et al.,  
159 2016) (Supplementary data-3). The ‘seed and grow’ algorithm works based on the difference in intensity of  
160 greyscale value in an image (Bright = minerals, dark = pores). After automatic segmentation, individual pores in  
161 SE2 images are manually corrected if required.

162 Similarly, using ImageJ software (threshold toolbox and machine learning algorithm), segmentation of the  
163 individual mineral phases was carried out combining BSE images and EDX elemental maps. While quartz, calcite,  
164 pyrite, mica minerals are efficiently segmented using these tools, feldspars are found difficult to segment because  
165 of similar composition as clay (Supplementary data-4, 5 and 6). Finally, corrected pore segmented SE2 mosaics  
166 are overlaid on the phase maps using the ‘georeference’ tool of QGIS (<http://qgis.osgeo.org>), (Supplementary data-  
167 4, 5 and 6).

168 [Pore detection resolution \(PPR\) and representative area analysis \(REA\)](#)

169 ‘Practical pore detection resolution’ (PPR) indicates the pore sizes above which one can assume to detect 100%  
170 of the pores present in the SE2 mosaic (Klaver et al., 2012). In agreement with earlier results using this instrument  
171 (Klaver et al., 2012; 2015; 2016; Hemes et al., 2013; 2015; 2016; Laurich et al., 2014), we found PPR of  $\sim 2000$



172 nm<sup>2</sup> and ~8500 nm<sup>2</sup> for the magnification of 20,000x and 10,000x images, respectively, corresponding to 10pixel  
173 size in an image.

174 After segmenting all minerals, representative elementary area analysis (REA) was performed using the box  
175 counting technique on mineralogical phase maps (Kameda et al., 2006; Klaver et al., 2012). Similar steps are also  
176 followed for determining a representative elementary area for SE2 images. The estimated REA values using SE2  
177 and BSE mosaics for the analysed 33 mudstone samples are documented in Supplementary data-7.

178 [Ion polishing and SEM technique \(second set of samples; BEG, UT Austin\).](#)

179 22 Samples (SN-34 to SN-55 in Table-1) were taken shipboard from the sample half of the still-wet core in small  
180 plastic tubes (similar to the ones used for the sample set at Aachen) inserted into the core by manual pressure. The  
181 tubes were removed from the core and sealed in plastic bags. In the laboratory at the BEG, sample bags were  
182 opened and the muds were allowed to dry slowly in the tubes over several weeks. No discernible shrinkage was  
183 observed as the dried core pieces still fully filled the tubes. The tubes were carefully removed and a small cube  
184 (approximately 0.5 to 1 cm<sup>3</sup>) was cut using a sharp knife and small hand saws; an orientation mark was placed on  
185 the cube to indicate the bedding direction. Bed-perpendicular surfaces were prepared by Ar-ion cross-section  
186 polishing, using the Leica EM TIC020 triple ion beam miller and coated with Ir for imaging. Manual placement  
187 of the cut cubes into the ion mill is not precise so the ion-polished surfaces have slight variation from perpendicular  
188 to bedding. Pore imaging was performed on the FEI Nova NanoSEM 430 using the in-lens SE detector, a 30 µm  
189 aperture, 15 KeV accelerating current, a working distance of around 5–6 mm, and an intermediate-range sample  
190 current (spot size = 3, mid-range for the instrument). Randomly selected views (typically 3-6) of all samples were  
191 collected at 6kx machine magnification; additional views illustrating pore types and pore/grain relationships were  
192 made at 10kx to 30kx (machine magnification).

## 193 Results

### 194 [Estimating compaction strain from MAD-porosity data](#)

195 Shipboard MAD (moisture and density) porosity versus depth data for mud samples exhibits a sharp reduction in  
196 porosity from 80% to 52% from the seafloor to 28 mbsf (Fig.2a). Deeper samples display a comparatively smaller  
197 reduction in porosity of approximately from 52% to 30% over a depth range of 28 to 1500 mbsf (Fig.2a and b).

198 We calculated compaction strain using the shipboard MAD porosity data following a method proposed by Nollet  
199 et al., 2005, and subsequently used by Neagu et al., 2010 (Fig.2c and d), assuming 1D consolidation and no change  
200 in solid volume. The compaction strain ( $\epsilon_c$ ) is then computed as:

$$201 \quad \epsilon_c = \frac{1-\phi_0}{1-\phi_1} \quad (\text{Eqn-1})$$

202 Here  $\phi_0$  = initial porosity, and  $\phi_1$  = final porosity. Our samples from sites U1480 and U1481 show no evidence of  
203 tectonic faults (McNeill et al., 2017), supporting our assumptions. We considered the initial porosity  $\phi_0$  as the  
204 MAD porosity at 0.6 mbsf depth ( $\phi_0 = 80\%$ ). Compaction strain following Eqn-1 (Supplementary data-7), is



205 plotted against depth in Fig. 2c and d. Compaction strain increases from 1 to 2.05 from the seafloor to 28 mbsf  
206 (i.e. Unit I), and from 2.00 to 3.05 from 28mbsf to 1500 mbsf (Fig. 2c and d).

207 Another common measure of compaction is the intergranular volume (IGV; Paxton, 2002), which corresponds to  
208 the sum of intergranular porosity and intergranular cement. In some mudstones, it may be necessary to calculate  
209 IGV differently because of the presence of abundant primary intragranular pores and pore-filling bitumen  
210 (Milliken and Olson, 2017). In our sample set, cement is absent, and IGV is taken to equal the bulk porosity from  
211 shipboard MAD measurements.

212 Compactional porosity loss (COPL), referenced against the original sediment volume, is calculated from the initial  
213 primary intergranular porosity ( $P_i$ ; 80% in this case) and the IGV as follows (Lundegard, 1992; Ehrenberg, 1989):

$$214 \text{ COPL} = P_i - \left( \frac{(100 - P_i) \times \text{IGV}}{100 - \text{IGV}} \right) \quad (\text{Eqn-2})$$

215 At an IGV of 50%, COPL is 60%; in the deepest samples in the Nicobar fan (IGV of around 30%) COPL is 70%  
216 (supplementary data-7). Contribution of cementation (CEPL) is absent in the absence of observed cements.

### 217 Description of grain microstructure and pore morphology

218 To have consistency in the data set, we prepared SE2 mosaics for all samples from the Aachen sample set at  
219 20,000x magnification covering an average  $100 \times 100 \mu\text{m}^2$  area (Supplementary data-7). In addition, to examine  
220 the effect of magnification on BIB-SEM porosity and representative area analysis (REA), three samples (i.e. SN-  
221 7, SN-15, and SN-29) were also imaged each at 5,000x and 10,000x magnification (Supplementary data-7),  
222 respectively. A decrease in magnification and resolution reduces visible BIB-SEM porosity.

223 We observed consistent results for the REA analysis. For SE2 mosaics REA varies between  $45 \times 45 \mu\text{m}^2$  to  $85 \times 85$   
224  $\mu\text{m}^2$  at 20,000x magnification, and for segmented phase maps, REA varies between  $90 \times 90 \mu\text{m}^2$  to  $130 \times 130 \mu\text{m}^2$   
225 at 10,000x magnification (Supplementary data-7). In the UT sample set, the standard images taken at 6kx with  
226 machine magnification are  $49.7 \times 45.7 \mu\text{m}^2$ , so these images are also within the estimated REA range.

227 Six mineral phases occur in significant amounts in the Sumatra samples, as detrital particles: quartz, feldspar (K-  
228 feldspar, albite, and Ca-plagioclase), calcite, micas (muscovite, biotite, and chlorite), and detrital clay clay-size  
229 particles, which are dominantly illite. The average clay percentage in these mudstone samples varies between 65%  
230 to 75%. Samples SN-1 (77%) and SN-4 (76%) are slightly enriched in clay content, whereas SN-7, SN-9, SN-17,  
231 SN-28, SN-29, and SN-31 contain less clay (<65%) (Supplementary data-7).

232 Using BIB-SEM and automatic pore segmentation techniques, an average of >30,000 pores have been detected  
233 for each individual sample in the Aachen sample set at 20,000x magnification. Correlating with the MAD data set,  
234 the estimated BIB-SEM porosity reduces from 32% to 19% over a depth range of seafloor to 28 mbsf, while the  
235 deeper samples display a smaller reduction from 19% to 10% over a depth range of 28 to 1500 mbsf respectively  
236 (Fig.3a). Consistent with numerous previous studies, the results document a mismatch between bulk measured  
237 porosity (MAD) and imaging porosity (BIB-SEM) (e.g., Hemes et al., 2013; Houben et al., 2014; Nole et al., 2016;



238 Olkar et al., 2019) (Supplementary data-7). We plotted BIB-SEM porosity vs MAD porosity and found an  
239 approximately linear correlation (Fig. 3b).

#### 240 Type of pores

241 Intergranular pores contribute >99% of the total visible porosity (Fig.4). Intragranular pores (see below) are rare.  
242 The size and shape of inter-granular pores change during compaction (Table 2).

243 Intergranular pores are classified based on grain size (irrespective of mineralogy): 1) Clay domain (matrix) pores,  
244 and 2) Silt-adjacent pores. Based on the variation in size, clay domain pores divided further into: 1) Large clay  
245 domain pores; pore size  $>5 \times 10^5 \text{ nm}^2$ , and the pore boundary is defined by more than three clay particles, and 2)  
246 small clay domain pores; the pore size  $<5 \times 10^5 \text{ nm}^2$  and generally occur in between two/three clay particles (see  
247 further detail below). Large and small clay domain pores are classified by geometry as: 1) Elongate pores (aspect  
248 ratio  $>3:1$ ) and, 2) equant-shaped pores (aspect ratio  $<3:1$ ). Elongate pores consist of: 1) linear-elongated pores,  
249 and 2) crescent-shaped elongated pores. Examples of different clay-domain pore types are shown in Fig. 5, 6, and  
250 7.

251 Silt-adjacent are categorized as two types: 1) large silt-adjacent pores are  $>5 \times 10^5 \text{ nm}^2$ , and pore boundaries are  
252 defined by more than three particles; and 2) small silt-adjacent pores include pore sizes  $<5 \times 10^5 \text{ nm}^2$ , and pore  
253 boundaries are defined by two/three particles (see further detail on the modal sizes of these pore types below).  
254 Large and small silt-adjacent pores are either: 1) Equant shaped (aspect ratio  $<3:1$ ) or 2) elongated (aspect ratio  
255  $>3:1$ ). Further, elongated silt-adjacent pores consist of: 1) linear-shaped elongated pores and 2) crescent-shaped  
256 elongated pores. These pore types are highlighted in Fig. 5, 6, and 7.

#### 257 Change in inter-particle pore morphology with depth

##### 258 *Seafloor to 28mbsf (Unit I)*

259 The shallow mud samples in Unit I are unconsolidated and highly porous (Fig. 5a; Supplementary data 8). Sample  
260 SN-1 (1.24 mbsf) has a maximum MAD porosity of 80%. We observe three types of clay particle contacts in the  
261 microstructure of SN-1; edge to edge (EE), edge to face (EF), and face to face (FF) contacts. Among them, EF and  
262 FF contacts are abundant and EE contacts are rare (Table 1). The sample exhibits abundant large clay domain  
263 pores and large silt-adjacent pores that are equant with smooth edges and a rounded pore perimeter. The sample  
264 also contains abundant linear-elongated and equant-shaped small clay-domain pores. Crescent-shaped small clay  
265 domain pores are rare in the microstructure of this sample. Equant-shaped, small silt-adjacent pores are abundant.  
266 In addition, linear elongated and crescent-shaped small, silt-adjacent pores are also commonly observed (Fig.5a;  
267 Table 2).

268 With increasing compaction strain ( $\epsilon_c = 1.119$ ) and depth (5.1 mbsf; Supplementary data 8), porosity (MAD)  
269 reduces to 75% and corresponding COPL=19% (sample SN-2; Fig. 5b). The microstructure of SN-2 displays  
270 almost similar characteristics as observed in the earlier sample SN-1, although there are fewer large clay domain  
271 pores in SN-2 than SN-1. Linear elongated and equant-shaped small clay domain pores are common (Table 2), but





272 crescent-shaped small clay domain pores are rare. The microstructure of SN-2 exhibits abundant equant-shaped  
273 large and small silt-adjacent pores.

274 With an increase in compaction strain to  $\epsilon_c \sim 2.00$  (28 mbsf), the sample microstructure is dominated by FF contacts  
275 (Fig. 5c), and EE and EF contacts are rare (Table 3). Additionally, large clay-domain pores become sparse or  
276 infrequent in the microstructure (Fig. 8). Crescent-shaped, small clay domain pores in the microstructure are rare,  
277 whereas equant-shaped small clay domain pores are common. Both small and large silt-adjacent pores exhibit  
278 equant shapes (Fig. 8d, e and f). The sample analysed at the base of Unit I (SN-6; 28 mbsf) contains rare large  
279 clay-domain pores and abundant FF contacts (Fig. 5c; MAD porosity = 54% and COPL = 55%).

#### 280 *28 mbsf to 1500 mbsf (Units II and III)*

281 Mud samples from the lower part of the Nicobar fan section are more compacted than shallower samples. We  
282 analyzed a total of 29 samples using BIB-SEM at Aachen and 18 samples using the field emission SEM at UT  
283 Austin from this section. An increase in compactional strain from 2.00 to 3.15 over a depth range of 28 to 1500  
284 mbsf causes a porosity reduction (MAD) of 54% to 28%, and the corresponding change in average COPL is 55%  
285 to 72%. The microstructure of these samples is dominated by FF contacts among clay particles; EF and EE contacts  
286 are rare (Table 3; Fig. 6 and 7 b, c). All samples exhibit abundant small linear-elongated clay domain pores between  
287 two parallel clay sheets (Fig. 8b). Equant-shaped small, clay domain pores are rarely observed below 150 mbsf  
288 depth ( $\epsilon_c > 2.4$ ). Crescent-shaped, small, clay domain pores are rare at shallow depth but become abundant with an  
289 increase in compactional strain  $\epsilon_c > 2.95$  (871.87 mbsf) as the surrounding clay particles are bent (Fig.6;  
290 Supplementary data 9). In addition, large clay domain pores in these samples are rarely observed in the vicinity of  
291 silt clasts (Table 2).

292 Below 100 mbsf ( $\epsilon_c = 2.20$ ), silt-adjacent small pores are dominantly equant shaped, but below 300 mbsf ( $\epsilon_c > 2.5$ )  
293 silt-adjacent small pores are dominantly linear-elongated (Fig. 8e). Crescent-shaped, small, silt-adjacent pores are  
294 common in all samples. Large silt-adjacent pores are dominantly equant above 200 mbsf depth ( $\epsilon_c < 2.40$ ) and  
295 commonly linear-elongate below 400 mbsf depth ( $\epsilon_c > 2.5$ ) (Fig.8f). It appears that due to an increase in  
296 compactional strain the shape of the silt-adjacent pores changes from equant to linear-elongated (Table 2). In  
297 samples with more silt, equant-shaped small and large, silt-adjacent pores can persist at greater depths (Fig. 8e and  
298 f).

299 Below 28 mbsf ( $\epsilon_c > 2.0$ ), the number of large silt-adjacent pores in the microstructure decreases. Comparing  
300 samples SN-8 (74.07 mbsf and  $\epsilon_c = 2.09$ ) and SN-32 (1267.14mbsf and  $\epsilon_c = 3.15$ ) illustrates how the number of  
301 large, silt-adjacent pores decreases with depth (Fig. 6a, and c) when the clay fraction (Supplementary Data 7) is  
302 comparable. This relationship is apparent even in samples separated by a smaller depth difference (SN-49 from  
303 959.14 mbsf and SN-55 from 1433.36 mbsf; Fig. 7b and c). While the number of large pores diminishes, the  
304 maximum size of the large silt-adjacent pores remains constant ( $10^7 \text{ nm}^2$ ; Supplementary data 10).



### 305 Intra-particle and intra-crystalline pores

306 Intraparticle pores are observed in microfossils, authigenic pyrite framboids, equant-shaped dolomite, calcite,  
307 quartz, mica, and lithic grains. Two different types of intraparticle pores were found in microfossils; elongated  
308 pores (Supplementary data 11a and c) and large rounded pores (Supplementary data 11b and d). The typical size  
309 of the elongated and Rounded pores in microfossils ( $10^5 \text{ nm}^2$ ) are larger than elongated pores ( $10^3 \text{ nm}^2$ ). While  
310 intraparticle pores in microfossils and most detrital grains are present at deposition, intraparticle pores in many  
311 mica grains form during burial and are considered secondary pores. Intraparticle pores in micas have cleavage-  
312 parallel, elongated pores with an aspect ratio  $>7$  (Supplementary data 11e), and are interpreted to open by bending  
313 of the micas during compaction (Supplementary data 11f).

### 314 Variation in the orientation of pores and grains due to compactional strain

315 We examined the change in orientation of the long axis of pores with increasing compaction strain. For all  
316 segmented pores, the angle between the long axis and the bedding plane was determined and plotted in rose  
317 diagrams (Supplementary data-12). Samples from the seafloor to 28 mbsf exhibit a weak preferred orientation of  
318 the long axis of pores with maxima oriented obliquely to the bedding planes. However, below 28 mbsf the samples  
319 have a preferred orientation of the long axis of pores aligned subparallel to the bedding plane. Further, due to an  
320 increase in vertical effective stress down section below 28 mbsf in Units II and III, the degree of preferred  
321 alignment of the long axis of pores only increases a small amount (Supplementary data-12).

322 We determined the angle between the long axis of individual silt grains and the bedding plane for all samples and  
323 plotted the angle in a rose diagram (Supplementary data-12). For quartz, feldspar, and calcite the degree of  
324 preferred orientation of the long axis of grains changes little with depth. However, the rose diagrams obtained for  
325 mica show a weak maxima parallel to the bedding plane and several submaxima oriented obliquely to the bedding  
326 plane above 28 mbsf. Preferred alignment of the long axis of mica grains increases at 28 mbsf with a strong  
327 maximum oriented parallel to bedding plane. Below 28 mbsf, further increase in the degree of preferred alignment  
328 is small.

### 329 Size distribution of pores

330 Pore size distributions (Fig.9) of shallow samples (Unit I) are trimodal. Sample SN-1 has peaks between  $10^5$  to  
331  $10^6 \text{ nm}^2$ ,  $10^6$  to  $10^7 \text{ nm}^2$ , and  $10^7$  to  $10^8 \text{ nm}^2$ , and SN-2 has peaks from  $10^4$  to  $10^5 \text{ nm}^2$ ,  $10^5$  to  $10^6 \text{ nm}^2$ , and  $10^6$  to  
332  $10^7 \text{ nm}^2$ . These three pore size regimes correspond to the small clay domain and silt-adjacent pores, large clay  
333 domain pores, and large silt-adjacent pores. Samples from Units II and III exhibit bimodal pore size distributions  
334 (SN-10, SN-26, and SN-33 in Fig.9). SN-10 has a peak between  $10^5$  to  $10^6 \text{ nm}^2$ , corresponding to small clay  
335 domain and silt-adjacent pores, and  $10^6$  to  $10^7 \text{ nm}^2$ , reflecting large silt-adjacent pores. Large clay domain pores  
336 are absent from samples below 28mbsf depth (Units II and III) based on the pore size distributions combined with  
337 image analysis. At the shallow depth, contribution to total porosity by larger silt adjacent pore is greater compared  
338 to the contribution by small clay domain pores (Fig.9 e and g). The contribution of large, silt-adjacent pores to  
339 total porosity diminishes with depth. Hence, at greater depth, contribution to total porosity by larger silt adjacent  
340 pore is less compared to small clay domain pores (Fig.9i).



341 Pore size distributions follow a power-law shown on a double logarithmic graph following the equations (Klaver  
342 et al., 2012; 2015; 2016; Hemes et al., 2013; 2015; 2016; Laurich et al., 2014):

$$343 \frac{N_i}{b_i S_{mosaic}} = C S_{pore}^D \quad (\text{Eqn-3})$$

$$344 \log\left(\frac{N_i}{b_i S_{mosaic}}\right) = -D \cdot \log(S_{pore}) + \text{Log } C \quad (\text{Eqn-4})$$

345 Where  $N_i$ = number of pores with area  $S_{pore}$ ,  $b_i$ = bin size,  $S_{mosaic}$ = surface area of the current mosaic,  
346  $C$ =constant, and  $D$ = power-law exponent. The resulting power-law exponent ( $D$ ) varies between 1.70 to 2.00  
347 (Supplementary data-7).

#### 348 [Effect of texture on porosity, pore morphology, and orientation of pores](#)

349 We analyzed six samples (SN-7, SN-9, SN-17, SN-28, SN-29 and SN-31) that are enriched in silt content compared  
350 to the rest of the mud samples (Supplementary data-7). Silt content has a positive correlation to the total SEM  
351 porosity. For example, sample SN-29 (1172.88 mbsf) exhibits a BIB-SEM porosity of 14% whereas other samples  
352 from a similar depth with less silt exhibit an average BIB-SEM porosity of 12% (Supplementary data-7) at 20000x  
353 magnification. The samples with greater silt content are also enriched in equant-shaped silt-adjacent larger pores  
354 (Supplementary data 13a). We also estimated the orientation of the long axis of pores for these three samples and  
355 plotted the obtained results as rose diagrams (Supplementary data 13b). The obtained results exhibit a relatively  
356 weak preferred alignment of the long axis of pores with respect to the bedding planes (Supplementary data 11b).

## 357 [Discussions](#)

### 358 [Effective stress vs porosity: A comparison with experimental study](#)

359 To understand the consolidation mechanisms of the Sumatra sediment we estimated vertical effective stress  
360 following the steps proposed by Hüpers et al., 2015. Following Tarzaghi and Peck (1948) vertical effective stress  
361 is expressed as:

$$362 \sigma_v' = \sigma_v - P_f \quad (\text{Eqn-7})$$

363 Here  $\sigma_v$  = total vertical stress caused by the overburden load, and  $P_f$  = fluid pressure. To compute vertical effective  
364 stress of a layered sediment, we use Eqn 8:

$$365 \sigma_v' = \sum(\rho_s - \rho_w) \cdot g \cdot \Delta z \quad (\text{Eqn-8})$$

366 where  $\rho_s$ = bulk density of the sediment,  $\rho_w$ = density of the pore water,  $\Delta z$ = depth interval, and  $g$ = gravitational  
367 acceleration. During IODP Expedition 362, drilling was performed 255 km away from the deformation front.  
368 Although small offset strike-slip faults are evident at the seafloor and in seismic reflection profiles (McNeill et al.,  
369 2017), the amount of strain attributed to these fault offsets is compatible with the idea that the maximum  
370 horizontal stress is comparable to the vertical stress; there is no evidence in seismic reflection data or from core



371 microstructures for thrust or reverse faults associated with a vertical least principal stress. On this basis, we assume  
372 that vertical effective stress is the maximum principal stress. Bulk density of the sediment  $\rho_s$  was obtained from  
373 McNeill et al., (2017), and  $\rho_w$  was considered as the density of sea-water i.e. 1025 kg/m<sup>3</sup> (Hüpers et al., 2015).

374 We plotted vertical effective stress vs MAD porosity of 55 mud samples (Fig. 10). Fawad et al. (2010)  
375 experimentally studied the consolidation behavior of mud with varied proportions of silt and clay. While Sumatra  
376 samples follow trends similar to those defined by Fawad et al. (2010), the experimental samples are more  
377 compacted than natural Sumatra samples for the same silt content.

378 Clay mineralogy has a significant effect on the compaction behavior of mudstone (Mondol et al., 2007). Mondol  
379 et al. (2007) performed compaction experiments using pure smectite and pure kaolinite clay particle packs; as they  
380 represent two end members compared to other clay minerals (illite and chlorite) in terms of grain size and surface  
381 area. Smectite is the most fine-grained clay and has the largest surface area; whereas kaolinite is the coarsest one  
382 and has smaller surface area among all other clay mineral types (Meade, 1963; Mesri and Olson, 1971; Rieke and  
383 Chilingarian, 1974). Hence, kaolinite is more compressible than smectite, and clay compaction gradually decreases  
384 with increasing the proportion of small size clay particles in the sample (Mondol et al, 2007).

385 Fawad et al., (2010) used clay mixtures of 81% kaolinite, 14% mica, and 5% microcline grains, whereas Sumatra  
386 mud samples are mainly composed of >73% of illite and lesser smectite, with only <16% undifferentiated chlorite  
387 and kaolinite, and <7% quartz particles. Therefore, due to higher illite/smectite content, Sumatra muds appeared  
388 to be less compacted compared to the experimental samples used by Fawad et al. (2010).

#### 389 BIB-SEM porosity vs MAD porosity

390 We note that BIB-SEM porosity is lower than the porosity found from the shipboard MAD data, however the two  
391 measurements correlate along a line through the origin. (Fig.3b). The reason for this difference is that MAD  
392 porosity measures the total amount of moisture in a much larger sample and accounts for pores much below the  
393 PPR and also rare large pores not included in the 1 mm<sup>2</sup> BIB section. Earlier studies also documented and discussed  
394 mismatch between MAD and BIB-SEM measurements (Hemes et al., 2013; Houben et al., 2014; Nole et al., 2016;  
395 Olkar et al., 2019). We plotted estimated BIB-SEM porosity and MAD porosity data from earlier studies on BOOM  
396 clay (Hemes et al., 2013; Olkar et al., 2019); Opalinus clay (Houben et al., 2014); and samples from Nankai trough  
397 (Nole et al., 2016). The data for Boom clay and Opalinus clay follow similar trend as Sumatra samples, whereas  
398 clay samples from Nankai trough shows different trend, and it could be attributed due to the difference in  
399 magnification of imaging of Nankai samples.

400 In addition we plotted clay content vs the difference between the two porosities in Supplementary data 14a. We  
401 performed regression analysis using the data set for the 33 muds samples analyzed at Aachen (Supplementary data  
402 14b). First, only two variables i.e., BIB-SEM porosity vs MAD porosity (following Eqn-5); second, we considered  
403 three variables MAD porosity, BIB-SEM porosity, and clay content (following the Eqn-6).

404 BIB-SEM porosity = a \* MAD porosity + c (Eqn-5)



405  $\text{BIB-SEM porosity} = a \cdot \text{MAD porosity} + b \cdot \text{clay content} + c$  (Eqn-6)

406 The coefficient of determinations ( $R^2$ ) for Eqn-5 and Eqn-6 are 0.8408 and 0.9262 respectively. These results  
407 show that the ratio in porosity depends on depth and clay content.

408 For all samples the BIB-SEM pore size distribution follows power-law over an interval of three orders of  
409 magnitude. We may extrapolate this below the practical pore resolution (PPR). (Klaver et al., 2012; Kuila and  
410 Prasad, 2013; Wang et al., 2019). Extrapolating our data set down to 3nm pore diameter, it is found that BIB-SEM  
411 porosity increases only up to 20%~25%. So, there is still an average mismatch of 15% to 20% between the MAD  
412 porosity and extrapolated BIB-SEM porosity. The fall off from the normal trend in log-log pore size distribution  
413 plots (Fig.9b) for the shallow depth (Unit-I) samples suggest that also large pores are uncounted in the data set.  
414 The mud samples from Unit-I contains forams that are rare or absent in the deeper section (Supplementary data-  
415 11a, b, c, and d), and missing pore volume can be attributed to the intact forams that may be missed due to the  
416 small size of the BIB SEM sample. Moreover, shallow depth samples are richer in smectite compared to the deeper  
417 samples, which can also somewhat influence to overestimate the MAD porosity.

#### 418 [Micromechanical model for porosity reduction](#)

##### 419 [Sharp reduction in porosity at the shallow depth from the seafloor to 28 mbsf](#)

420 High porosity (80% MAD; 32% BIB-SEM) in the shallowest sediments is attributed to large pores in the samples  
421 created by abundant EE and EF particle contacts (Fig. 5a and 7a). These contacts are unstable and collapse to form  
422 FF contacts, resulting in a rapid porosity decrease with 28m of burial (Table 3). This deformation is apparent from  
423 the reduction in large clay domain pores observed over this interval (Fig. 8; Table 2). Collapse of pores surrounded  
424 by EE and EF contacts is further recognized by the progressive alignment of clay particles into the bedding plane  
425 and by the increase number and consistent orientation of elongated, small, clay domain pores. Each of these  
426 observations is consistent with rotation of clay particles into the bedding plane as these large clay domain pores  
427 collapse.

##### 428 [Mechanism of porosity reduction from 28 mbsf to 1500 mbsf](#)

429 Below 28 mbsf to >1500 mbsf, porosity continues to decrease from 50-32% (MAD) but at a reduced pace. SEM  
430 observations suggest that this porosity decline results from the progressive loss of silt-adjacent pores with large  
431 silt-adjacent pores lost before small ones (Fig. 8), although they remain present in common abundance to 1200  
432 mbsf. Small, clay domain pores are abundant throughout the section, and the large clay domain pores were lost  
433 above 28 mbsf.

434 Within the population of silt-adjacent pores, the large, equant pores are most susceptible to collapse (Fig. 8). Large,  
435 elongate pores persist in abundance, both in linear and crescent geometries. While it seems plausible that large,  
436 equant pores collapse to form large, elongate pores, no corresponding increase in the elongate pore population is  
437 observed. Large, elongate pores may collapse further and become small silt-adjacent pores. Microstructural  
438 evidence supports the idea that large equant pores collapse as surrounding clay aggregates bend and shrink the size  
439 of the remaining pore (Fig. 11a to f), and that the collapse results in an increasing aspect ratio of the pore. While



440 initial pore shrinkage may be accommodated solely by the bending of clay particles above the pore (Fig. 11),  
441 further collapse may require clay particles to slide into the pore (Fig.11g-iii) or become fractured (Fig.11g-v) in  
442 order to allow clay to invade the pore (model shown in Fig.11 is elaborately described in Supplementary data-15).

443 Small, silt-adjacent pores also become less abundant with burial, but the transition occurs deeper than the large  
444 pores, and small, silt-adjacent pores remain common throughout the section (Fig. 11). Equant, small pores are lost  
445 like the large pores, and elongate pores remain abundant within this population subset throughout. There is a loose  
446 correspondence between the loss of small, equant pores and an increase in elongate pores, suggesting that pore  
447 flattening is part of the pore collapse history. The pore collapse evolution outlined for large pores (Fig. 11) appears  
448 to hold for small pores, even though observations are more challenging.

449 Small, clay domain pores appear to remain resilient throughout the compaction history (Fig. 8), even though some  
450 of these pores must become lost to account for porosity loss. Small, equant pores are lost between 100-200 m, and  
451 this loss appears to be accommodated by an increase in elongate pores (Fig. 8). Elongate crescent pores increase  
452 in abundance around 800 mbsf, and we interpret this to reflect folding of abundant linear elongate pores as the  
453 overall system compacts.

454 Large, equant pores in the clay domain are lost within the first few 10's of meters of burial. Elongate pores appear  
455 to form at the expense of equant pores, and there may be a reduction in pore size associated with this shape change.  
456 Most of the pores remaining after 1500 m of burial are small, elongate pores found both in clay domain and silt-  
457 adjacent pores.

458 The presence of silt particles locally redistributes the force chain of load to retain silt-adjacent, large pores  
459 undeformed (Schneider et al., 2011). The samples with greater silt content are also enriched in equant-shaped silt-  
460 adjacent larger pores (Supplementary data 13a) in the microstructure. Hence, and as a result, they display greater  
461 porosity compared to other samples from similar depths intervals (Supplementary data-7).

462 Previous laboratory studies have emphasized the importance of clay particle rotation as a dominant mechanism for  
463 mechanical compaction in mudstone (Bennett et al., 1981; Vasseur et al., 1995; Aplin et al., 2006; Day-Stirrat et  
464 al., 2008; 2011). While we infer rotation is an important mechanism for mechanical compaction at the shallowest  
465 depth where unstable EE and EF particle contacts are present, clay particle bending and sliding/fracturing are  
466 considered more important for most of the section studied.

#### 467 [Mechanical compaction of marine sediment: a conceptual model](#)

468 According to Emmanuel and Day-Stirrat (2020), the reduction of pores in sedimentary rocks during compaction  
469 is size-dependent; larger pores deform much readily than smaller pores. According to their model, larger pores  
470 rapidly decrease in size during compaction to reduce the overall porosity of the sample. However, microstructural  
471 analysis of Sumatra samples suggests that porosity reduction is accomplished by compaction of all pore sizes.  
472 While large, clay domain pores are lost more quickly than large, silt-adjacent pores, silt-adjacent pores are larger  
473 than clay domain pores. Moreover, the maximum size of pores remains almost constant irrespective of increasing  
474 vertical effective stress/depth (Supplementary data 8) with little difference observed for the maximum pore size in



475 samples from 98.25 mbsf and 1299.31 mbsf. The preservation of a constant ratio between MAD and BIB-SEM  
476 porosity measurements (Fig. 3b) suggests that porosity loss is distributed across all pore sizes. We infer that all  
477 pore sizes are available for compaction for every increment of applied stress but acknowledge that the rate of pore  
478 reduction in different size classes may proceed at different rates.

479 We propose a new model for the reduction in porosity in which, all pores within the force chain of load take part  
480 in the reduction in porosity during compaction irrespective of their size. At shallow depth up to 28mbsf, larger  
481 clay-domain pores are the most susceptible to early response during an increase in compactional strain; because  
482 of two reasons- 1) the ‘domains’ defined by the clay aggregate are weaker compared to the larger rigid silt grains,  
483 and 2) due to higher relative proportion of clay-rich regions within the mud, the force chain of load dominantly  
484 passes through the clay aggregate. The dispersed nature of the silt-size particles and the high proportion of  
485 phyllosilicates in the mud samples indicate that soft clay particles act as the principal load-bearing framework.  
486 Hence, larger clay domain pores are more unstable compared to silt adjacent pores in the mud microstructure.  
487 Similarly, below 28mbsf depth in Units II and III, under an increase in vertical effective stress, both the larger silt-  
488 adjacent pores and smaller pores in the clay matrix that come within the force chain of load collapse. Hence, the  
489 ratio between BIB-SEM porosity vs MAD porosity remains almost constant irrespective of the depth. All larger  
490 silt-adjacent pores do not come within the force chain of load at the same time. Hence, some of the larger silt-  
491 adjacent pores remained undeformed to the maximum depth of 1500mbsf depth. Therefore, the maximum size of  
492 the larger silt adjacent larger pores remains almost constant irrespective of the depth/vertical effective stress.

493 While our understanding of how different pore types is consistent with all available data, tracking the pore  
494 evolution through additional size categories would elucidate the pore evolution in more detail. Preliminary pore  
495 size distribution data (Fig.9) indicate that 4 size bins exist in these samples. Developing this approach requires  
496 improved image analysis techniques to tie all the pore attributes together on a pore-by-pore basis for a huge number  
497 of pores.

#### 498 [Compaction strain accommodation and grain-scale deformation](#)

499 Deformation of clay-rich sedimentary rocks involves four possible mechanisms: 1) Particulate flow; (Morgenstern  
500 and Tchalenko, 1967; Borradaile et al., 1981); 2) Cataclasis; (Ukar and Cloos, 2019) 3) Diffusive mass transfer;  
501 (Blenkinsop, 2000; Fossen, 2016); 4) Intercrystalline plasticity (Blenkinsop, 2000; Fossen, 2016). The intensity  
502 and occurrence of a particular deformation mechanism in mudstone depend on several parameters, such as  
503 effective stress, water content, cementation, temperature (Desbois et al., 2017; Den Hartog and Spiers, 2014).

504 All our samples show evidence of particulate flow controlled by friction between grains. At shallow depths, illite  
505 platelets contacted at EE and EF junctions lose these weak bonds, and particles rotate into bedding-parallel  
506 orientation. Once FF contacts dominate, large-scale rotations are reduced and intra-crystalline slip becomes  
507 important. This is best evidenced in collapse of large, silt-adjacent pores where bent clay particles overlie pores  
508 (Fig.11). In deforming granular foam material, bending was reported as the dominant deformation mechanism for  
509 the reduction in porosity and developing preferred alignment of the long axis of pores perpendicular to the applied  
510 stress (Elliott et al., 2002, Zhou et al., 2004; Samsudin et al., 2017; Zakaria et al., 2018) (review of these earlier



511 studies on the experimental deformation of granular foam is described in supplementary data-16). Friction adheres  
512 clay particles to the edge of pores while the middle of particles drops into the pore, resulting in bending by intra-  
513 crystalline slip. A cartoon (Fig. 12g) illustrates the compaction mechanism associated with the bending of clay  
514 particles. With increasing compaction strain, clay particles undergo bending, and as a result, pore area reduces and  
515 the orientation of the pores tends to align perpendicular to the applied effective stress (Fig. 12g).

## 516 [Compaction of Sumatra input section: generalized implication for rock property](#) 517 [evolution](#)

518 The overall compaction curve obtained for Sumatra muds is comparable with the experimental study by Fawad et  
519 al., 2010 in the context of compactional range (Fig.8). The curve shows a monoexponential decrease in porosity  
520 with an increase in vertical effective stress, which is evidence of normal consolidation (Fawad et al., 2010;  
521 Dutilleul et al., 2020).

522 The larger silt-adjacent pores seen in the deepest of these samples (1500 m burial) suggest these muds retain  
523 considerable potential for additional compaction in deeper burial. As this marine sediment progressively  
524 approaches greater burial at closer proximity of the accretionary prism, it will undergo further change in physical  
525 and deformational properties (Bray and Karig, 1985). Despite the substantial compactional strain, the relatively  
526 high porosity of the deepest sample and the survival of larger and mechanically unstable silt-margin pores suggests  
527 that compactional stabilization has not been reached because such IGVs and pore types are not generally observed  
528 in older and lithified mudrocks. Based on the current understanding of subduction zone deformation behavior and  
529 mudrock properties, it seems likely that compaction will continue to dominate the pore loss in deeper burial.

530 The general absence of early cementation and the corresponding dominance of compaction in the total pore loss,  
531 is consistent with observations of other siliciclastic-dominated muds (Milliken, 2014; 2019). The trends for  
532 intergranular volume observed across the seafloor to 1500mbsf place useful constraints on the maximum cement  
533 volumes that theoretically could be emplaced at this depth range in sediments containing a more reactive grain  
534 assemblage. At the depths of burial attained at the deformation front, any cementation of the Sumatra input  
535 sediments will be limited to <30% of the rock volume, or possibly much less, as compaction is expected to continue  
536 up to the burial temperatures that initiate grain reactions and associated cementation.

## 537 [Conclusions](#)

538 Pores can be classified by size and also microstructural position. Their contribution to the total porosity is  
539 multimodal.

540 Samples at shallow depth (seafloor to 28 mbsf) display a sharp reduction in porosity from 80% to 52% due to the  
541 collapse of the large clay domain/matrix pores. Deeper samples (28 mbsf to 1500 mbsf) exhibit a smaller reduction  
542 in porosity from 50% to 32% due to collapse of silt-adjacent pores by bending and subsequently fracturing/sliding  
543 of clay aggregate.





544 Large equant pores in clay (between  $10^6$  and  $10^7$  nm<sup>2</sup>) are rare below the first few meters of burial, after the  
545 flocculated structure collapses.

546 The class of large pores next to silt-size grains (between  $10^4$  and  $10^6$  nm<sup>2</sup>) remains common to >1 km burial,  
547 irrespective of the mineralogy of the silt-sized grains, but their size decreases with depth. Small, equant pores next  
548 to silt particles are abundant in the first 100 m of burial and remain common over the whole samples depth range.

549 Small pores in clay domains are almost all elongated, and abundant over all observed depths. Small, crescent-  
550 shaped elongate pores increase in abundance with depth as clay particles become folded by compactional  
551 processes.

552 The size-independence of pore loss arises because the force chain driving pore collapse is localized primarily  
553 within the volumetrically dominant and weaker clay-rich domains; larger pores around isolated silt particles enter  
554 into the force chain somewhat randomly and asynchronously and do not contribute preferentially to pore loss over  
555 the depth range studied.

556 An increase in effective stress up to 18MPa (~1500 mbsf) causes the development of weakly aligned phyllosilicate  
557 fabric (defined by mica and illite clay particles) in the microstructure.

558 Compaction processes in our samples are dominated by granular flow (rotation and frictional sliding of illite clay  
559 particles) at shallow depths. With increasing depth, compaction is additionally accommodated by bending of clay  
560 particles.

## 561 Data availability

562 High resolution SE2 and BSE images of all samples are available online at:  
563 <https://figshare.com/s/cbaada517b0b1409d575>

## 564 Authors contributions

565 SL and KLM performed sample preparation and BIB-SEM microscopy. SL analysed the data. JLU and GD  
566 acquired funding. JLU managed the project. PV, KLM and JLU significantly contributed to interpret the data. SL  
567 wrote the first draft of the manuscript. PV, KLM and JLU contributed for the correction and improvement of the  
568 manuscript.

## 569 Competing interests

570 The authors declare that they do not have any conflict of interest.



## 571 Acknowledgments

572 SL and JLU thank German Research Foundation (Deutsche Forschungsgemeinschaft [DFG] grant UR 64/19-1)  
573 for providing funding to carry out the research. IODP (International Ocean Discovery Programme) sample  
574 repository, Japan is acknowledged for providing oriented mud samples for the study. KLM acknowledges the  
575 samples and data provided by the International Ocean Discovery Program (IODP). Funding for sample preparation  
576 and SEM imaging was supported by a post-expedition award (Milliken, P.I.) from the Consortium for Ocean  
577 Leadership. SL thanks Manuel Menzel, Jop Klaver, Liene Spruženiece, and Joyce Schmatz for providing valuable  
578 time to teach BIB-SEM techniques.

## 579 References

- 580 Ajdukiewicz, J. M. and R. H. Lander 2010. Sandstone reservoir quality prediction: state of the art. *AAPG Bulletin*  
581 94: 1082-1091.
- 582 Alam, M., Alam, M.M., Curray, J.R., Chowdhury, M.L.R. and Gani, M.R., 2003. An overview of the sedimentary  
583 geology of the Bengal Basin in relation to the regional tectonic framework and basin-fill history. *Sedimentary*  
584 *geology*, 155(3-4), pp.179-208.
- 585 Al-Mukhtar, M., Belanteur, N., Tessier, D., and Vanapalli, S.K. (1996). The fabric of a clay soil under controlled  
586 mechanical and hydraulic stress states. *Appl. Clay Sci.* 11, 99–115.
- 587 Ammon, C.J., Ji, C., Thio, H.K., Robinson, D., Ni, S., Hjorleifsdottir, V., Kanamori, H., Lay, T., Das, S.,  
588 Helmberger, D. and Ichinose, G., 2005. Rupture process of the 2004 Sumatra-Andaman  
589 earthquake. *science*, 308(5725), pp.1133-1139.
- 590 Aplin, A. C., I. F. Matenaar, D. K. McCarty and B. A. van der Pluijm 2006. Influence of mechanical compaction  
591 and clay mineral diagenesis on the microfabric and pore-scale properties of deep-water Gulf of Mexico mudstones.  
592 *Clays and Clay Minerals* 54: 514-500.
- 593 Aplin, A.C. and Yagiz, J.H., 2011. Mudstone diversity: Origin and implications for source, seal, and reservoir  
594 properties in petroleum systems. *AAPG bulletin*, 95(12), pp.2031-2059.
- 595 Aplin, A.C., Matenaar, I.F. and van der Pluijm, B., 2003. Influence of mechanical compaction and chemical  
596 diagenesis on the microfabric and fluid flow properties of Gulf of Mexico mudstones. *Journal of Geochemical*  
597 *Exploration*, 78, pp.449-451.
- 598 Aplin, A.C., Matenaar, I.F., McCarty, D.K. and van Der Pluijm, B.A., 2006. Influence of mechanical compaction  
599 and clay mineral diagenesis on the microfabric and pore-scale properties of deep-water Gulf of Mexico  
600 mudstones. *Clays and Clay Minerals*, 54(4), pp.500-514.



- 601 Backman, J., W. Chen, S. Kachovich, F. L. Mitchison, K. E. Petronotis, T. Yang and X. Zhao (2019). Data report;  
602 Revised age models for IODP Sites U1480 and U1481, Expedition 362. Proceedings of the International Ocean  
603 Discovery Program, Expedition Reports 362: 7.
- 604 Bennett, R.H., Bryant, W.R. and Keller, G.H., 1981. Clay fabric of selected submarine sediments; fundamental  
605 properties and models. *Journal of Sedimentary Research*, 51(1), pp.217-232.
- 606 Bennett, R.H., O'Brien, N.R. and Hulbert, M.H., 1991. Determinants of clay and shale microfabric signatures:  
607 processes and mechanisms. In *Microstructure of Fine-Grained Sediments* (pp. 5-32). Springer, New York, NY.
- 608 Bjørlykke, K. and Høeg, K., 1997. Effects of burial diagenesis on stresses, compaction and fluid flow in  
609 sedimentary basins. *Marine and Petroleum Geology*, 14(3), pp.267-276.
- 610 Bjørlykke, K., 1998. Clay mineral diagenesis in sedimentary basins-a key to the prediction of rock properties.  
611 Examples from the North Sea Basin. *Clay minerals*, 33(1), pp.15-34.
- 612 Blenkinsop, T.G., 2007. *Deformation microstructures and mechanisms in minerals and rocks*. Springer Science &  
613 Business Media.
- 614 Boisson, J.Y. (2005). *Clay Club Catalogue of Characteristics of Argillaceous Rocks* (OECD NEA No. 4436).
- 615 Borradaile, G.J., 1981. Particulate flow of rock and the formation of cleavage. *Tectonophysics*, 72(3-4), pp.305-  
616 321.
- 617 Bowles, F.A., Bryant, W.R. and Wallin, C., 1969. Microstructure of unconsolidated and consolidated marine  
618 sediments. *Journal of Sedimentary Research*, 39(4), pp.1546-1551.
- 619 Bray, C.J. and Karig, D.E., 1985. Porosity of sediments in accretionary prisms and some implications for  
620 dewatering processes. *Journal of Geophysical Research: Solid Earth*, 90(B1), pp.768-778.
- 621 Casagrande, A., 1932. Research on the Atterberg limits of soils. *Public roads*, 13(8), pp.121-136.
- 622 Casagrande, A., 1932. *The structure of clay and its importance in foundation engineering*. Boston Society Civil  
623 Engineers Journal.
- 624 Cetin, H., 2004. Soil-particle and pore orientations during consolidation of cohesive soils. *Engineering  
625 geology*, 73(1-2), pp.1-11.
- 626 Chester, F.M., Rowe, C., Ujiie, K., Kirkpatrick, J., Regalla, C., Remitti, F., Moore, J.C., Toy, V., Wolfson-  
627 Schwehr, M., Bose, S. and Kameda, J., 2013. Structure and composition of the plate-boundary slip zone for the  
628 2011 Tohoku-Oki earthquake. *Science*, 342(6163), pp.1208-1211.



- 629 Collins, K.T. and McGown, A., 1974. The form and function of microfabric features in a variety of natural  
630 soils. *Geotechnique*, 24(2), pp.223-254.
- 631 Cook, B.J., Henstock, T.J., McNeill, L.C. and Bull, J.M., 2014. Controls on spatial and temporal evolution of  
632 prism faulting and relationships to plate boundary slip offshore north-central Sumatra. *Journal of Geophysical  
633 Research: Solid Earth*, 119(7), pp.5594-5612.
- 634 Cubas, N., Souloumiac, P. and Singh, S.C., 2016. Relationship link between landward vergence in accretionary  
635 prisms and tsunami generation. *Geology*, 44(10), pp.787-790.
- 636 Curtis, C.D., Lipshie, S.R., Oertel, G. and Pearson, M.J., 1980. Clay orientation in some Upper Carboniferous  
637 mudrocks, its relationship to quartz content and some inferences about fissility, porosity and compactional  
638 history. *Sedimentology*, 27(3), pp.333-339.
- 639 Day-Stirrat, R.J., Aplin, A.C., Środoń, J. and Van der Pluijm, B.A., 2008. Diagenetic reorientation of phyllosilicate  
640 minerals in Paleogene mudstones of the Podhale Basin, southern Poland. *Clays and Clay Minerals*, 56(1), pp.100-  
641 111.
- 642 Day-Stirrat, R.J., Flemings, P.B., You, Y., Aplin, A.C. and van der Pluijm, B.A., 2012. The fabric of consolidation  
643 in Gulf of Mexico mudstones. *Marine Geology*, 295, pp.77-85.
- 644 Day-Stirrat, R.J., Milliken, K.L., Dutton, S.P., Loucks, R.G., Hillier, S., Aplin, A.C. and Schleicher, A.M., 2010.  
645 Open-system chemical behavior in deep Wilcox Group mudstones, Texas Gulf Coast, USA. *Marine and Petroleum  
646 Geology*, 27(9), pp.1804-1818.
- 647 Dean, S.M., McNeill, L.C., Henstock, T.J., Bull, J.M., Gulick, S.P., Austin, J.A., Bangs, N.L., Djajadihardja, Y.S.  
648 and Permana, H., 2010. Contrasting décollement and prism properties over the Sumatra 2004–2005 earthquake  
649 rupture boundary. *Science*, 329(5988), pp.207-210.
- 650 Den H, S.A. and Spiers, C.J., 2014. A microphysical model for fault gouge friction applied to subduction  
651 megathrusts. *Journal of Geophysical Research: Solid Earth*, 119(2), pp.1510-1529.
- 652 Desbois, G., Höhne, N., Urai, J.L., Bésuelle, P. and Viggiani, G., 2017. Deformation in cemented mudrock  
653 (Callovo–Oxfordian Clay) by microcracking, granular flow and phyllosilicate plasticity: insights from triaxial  
654 deformation, broad ion beam polishing and scanning electron microscopy. *Solid Earth*, 8(2), pp.291-305.
- 655 Desbois, G., Urai, J.L. and Kukla, P.A., 2009a. Morphology of the pore space in claystones—evidence from  
656 BIB/FIB ion beam sectioning and cryo-SEM observations. *eEarth Discussions*, 4(1), pp.1-19.
- 657 Desbois, G., Urai, J.L., Kukla, P.A., Konstanty, J. and Baerle, C., 2011. High-resolution 3D fabric and porosity  
658 model in a tight gas sandstone reservoir: A new approach to investigate microstructures from mm-to nm-scale  
659 combining argon beam cross-sectioning and SEM imaging. *Journal of Petroleum Science and Engineering*, 78(2),  
660 pp.243-257.



- 661 Desbois, G., Urai, J.L. and Kukla, P.A., 2009b. Morphology of the pore space in claystones—evidence from  
662 BIB/FIB ion beam sectioning and cryo-SEM observations. *eEarth Discussions*, 4(1), pp.1-19.
- 663 Desbois, G., Urai, J.L., Hemes, S., Brassinnes, S., De Craen, M. and Sillen, X., 2014. Nanometer-scale pore fluid  
664 distribution and drying damage in preserved clay cores from Belgian clay formations inferred by BIB-cryo-  
665 SEM. *Engineering Geology*, 179, pp.117-131.
- 666 Desbois, G., Urai, J.L., Hemes, S., Brassinnes, S., De Craen, M. and Sillen, X., 2014. Nanometer-scale pore fluid  
667 distribution and drying damage in preserved clay cores from Belgian clay formations inferred by BIB-cryo-  
668 SEM. *Engineering Geology*, 179, pp.117-131.
- 669 Díaz-Azpiroz, M., Brune, S., Leever, K.A., Fernández, C. and Czeck, D.M., 2016. Tectonics of oblique plate  
670 boundary systems. *Tectonophysics*, 693, pp.165-170.
- 671 Djéran-Maigre, I., Tessier, D., Grunberger, D., Velde, B. and Vasseur, G., 1998. Evolution of microstructures and  
672 of macroscopic properties of some clays during experimental compaction. *Marine and Petroleum Geology*, 15(2),  
673 pp.109-128.
- 674 Djéran-Maigre, I., Tessier, D., Grunberger, D., Velde, B. and Vasseur, G., 1998. Evolution of microstructures and  
675 of macroscopic properties of some clays during experimental compaction. *Marine and Petroleum Geology*, 15(2),  
676 pp.109-128.
- 677 Dugan, B., McNeill, L. and Petronotis, K., 2017. Expedition 362 preliminary report: Sumatra subduction  
678 zone. *International Ocean Discovery Program*.
- 679 Dutilleul, J., Bourlange, S., Conin, M. and Géraud, Y., 2020. Quantification of bound water content, interstitial  
680 porosity and fracture porosity in the sediments entering the North Sumatra subduction zone from Cation Exchange  
681 Capacity and IODP Expedition 362 resistivity data. *Marine and Petroleum Geology*, 111, pp.156-165.
- 682 Dutta, N.C., 1986. Shale compaction, burial diagenesis, and geopressures: A dynamic model, solution and some  
683 results. *Collection colloques et séminaires-Institut français du pétrole*, (44), pp.149-172.
- 684 Ehrenberg, S. N. 1989. Assessing the relative importance of compaction processes and cementation to reduction  
685 of porosity in sandstones: discussion. *American Association of Petroleum Geologists Bulletin* 73: 1274-1276.
- 686 Emmanuel, S. and Day-Stirrat, R.J., 2012. A framework for quantifying size dependent deformation of nano-scale  
687 pores in mudrocks. *Journal of applied geophysics*, 86, pp.29-35.
- 688 Fawad, M., Mondol, N.H., Jahren, J. and Bjørlykke, K., 2010. Microfabric and rock properties of experimentally  
689 compressed silt-clay mixtures. *Marine and Petroleum Geology*, 27(8), pp.1698-1712.
- 690 Fernandez-Blanco, D., Philippon, M. and von Hagke, C., 2016. Structure and kinematics of the Sumatran fault  
691 system in North Sumatra (Indonesia). *Tectonophysics*, 693, pp.453-464.



- 692 Fossen, H., 2016. Structural geology. Cambridge university press.
- 693 Geersen, J., McNeill, L., Henstock, T.J. and Gaedicke, C., 2013. The 2004 Aceh-Andaman Earthquake: Early clay  
694 dehydration controls shallow seismic rupture. *Geochemistry, Geophysics, Geosystems*, 14(9), pp.3315-3323.
- 695 Ghosal, D., Singh, S.C. and Martin, J., 2014. Shallow subsurface morphotectonics of the NW Sumatra subduction  
696 system using an integrated seismic imaging technique. *Geophysical Journal International*, 198(3), pp.1818-1831.
- 697 Gulick, S.P., Austin, J.A., McNeill, L.C., Bangs, N.L., Martin, K.M., Henstock, T.J., Bull, J.M., Dean, S.,  
698 Djajadihardja, Y.S. and Permana, H., 2011. Updip rupture of the 2004 Sumatra earthquake extended by thick  
699 indurated sediments. *Nature Geoscience*, 4(7), pp.453-456.
- 700 Guo, P. and Stolle, D.F.E., 2013. Coupled analysis of bifurcation and shear band in saturated soils. *Soils and*  
701 *foundations*, 53(4), pp.525-539.
- 702 Handy, M.R., 1994. Flow laws for rocks containing two non-linear viscous phases: a phenomenological  
703 approach. *Journal of Structural Geology*, 16(3), pp.287-301.
- 704 Hemes, S., Desbois, G., Klaver, J. and Urai, J.L., 2016. Microstructural characterisation of the Ypresian clays  
705 (Kallo-1) at nanometre resolution, using broad-ion beam milling and scanning electron microscopy. *Netherlands*  
706 *Journal of Geosciences*, 95(3), pp.293-313.
- 707 Hemes, S., Desbois, G., Urai, J.L., De Craen, M. and Honty, M., 2013. Variations in the morphology of porosity  
708 in the Boom Clay Formation: insights from 2D high resolution BIB-SEM imaging and Mercury injection  
709 Porosimetry. *Netherlands Journal of geosciences*, 92(4), pp.275-300.
- 710 Hemes, S., Desbois, G., Urai, J.L., De Craen, M. and Honty, M., 2013. Variations in the morphology of porosity  
711 in the Boom Clay Formation: insights from 2D high resolution BIB-SEM imaging and Mercury injection  
712 Porosimetry. *Netherlands Journal of geosciences*, 92(4), pp.275-300.
- 713 Hemes, S., Desbois, G., Urai, J.L., Schröppel, B. and Schwarz, J.O., 2015. Multi-scale characterization of porosity  
714 in Boom Clay (HADES-level, Mol, Belgium) using a combination of X-ray  $\mu$ -CT, 2D BIB-SEM and FIB-SEM  
715 tomography. *Microporous and mesoporous materials*, 208, pp.1-20.
- 716 Hesse, R., 1975. Turbiditic and non-turbiditic mudstone of Cretaceous flysch sections of the East Alps and other  
717 basins. *Sedimentology*, 22(3), pp.387-416.
- 718 Hippchen, S. and Hyndman, R.D., 2008. Thermal and structural models of the Sumatra subduction zone:  
719 Implications for the megathrust seismogenic zone. *Journal of Geophysical Research: Solid Earth*, 113(B12).
- 720 Ho, N.C., Peacor, D.R. and Van der Pluijm, B.A., 1999. Preferred orientation of phyllosilicates in Gulf Coast  
721 mudstones and relation to the smectite-illite transition. *Clays and Clay Minerals*, 47(4), pp.495-504.



- 722 Houben, M.E., Desbois, G. and Urai, J.L., 2013. Pore morphology and distribution in the Shaly facies of Opalinus  
723 Clay (Mont Terri, Switzerland): Insights from representative 2D BIB–SEM investigations on mm to nm  
724 scale. *Applied Clay Science*, 71, pp.82-97.
- 725 Houben, M.E., Desbois, G. and Urai, J.L., 2014. A comparative study of representative 2D microstructures in  
726 Shaly and Sandy facies of Opalinus Clay (Mont Terri, Switzerland) inferred from BIB-SEM and MIP  
727 methods. *Marine and Petroleum Geology*, 49, pp.143-161.
- 728 Hunze, S. and Wonik, T., 2007. Compaction in the Nankai and Barbados accretionary prisms: New insights from  
729 logging-while-drilling data. *Geochemistry, Geophysics, Geosystems*, 8(2).
- 730 Hüpers, A., Ikari, M.J., Dugan, B., Underwood, M.B. and Kopf, A.J., 2015. Origin of a zone of anomalously high  
731 porosity in the subduction inputs to Nankai Trough. *Marine Geology*, 361, pp.147-162.
- 732 Hüpers, A., Torres, M.E., Owari, S., McNeill, L.C., Dugan, B., Henstock, T.J., Milliken, K.L., Petronotis, K.E.,  
733 Backman, J., Bourlange, S. and Chemale, F., 2017. Release of mineral-bound water prior to subduction tied to  
734 shallow seismogenic slip off Sumatra. *Science*, 356(6340), pp.841-844.
- 735 Ikari, M.J., Niemeijer, A.R. and Marone, C., 2015. Experimental investigation of incipient shear failure in foliated  
736 rock. *Journal of Structural Geology*, 77, pp.82-91.
- 737 Illangasekare, T., Tyler, S.W., Clement, T.P., Villholth, K.G., Perera, A.P.G.R.L., Obeysekera, J., Gunatilaka, A.,  
738 Panabokke, C.R., Hyndman, D.W., Cunningham, K.J. and Kaluarachchi, J.J., 2006. Impacts of the 2004 tsunami  
739 on groundwater resources in Sri Lanka. *Water Resources Research*, 42(5).
- 740 Ingram, G.M. and Urai, J.L., 1999. Top-seal leakage through faults and fractures: the role of mudrock  
741 properties. *Geological Society, London, Special Publications*, 158(1), pp.125-135.
- 742 Jacob, G., Kisch, H.J. and van der Pluijm, B.A., 2000. The relationship of phyllosilicate orientation, X-ray  
743 diffraction intensity ratios, and c/b fissility ratios in metasedimentary rocks of the Helvetic zone of the Swiss Alps  
744 and the Caledonides of Jaemtland, central western Sweden. *Journal of Structural Geology*, 22(2), pp.245-258.
- 745 Jessell, M.W., Bons, P.D., Grier, A., Evans, L.A. and Wilson, C.J., 2009. A tale of two viscosities. *Journal of*  
746 *Structural Geology*, 31(7), pp.719-736.
- 747 Jiang, M., Klaver, J., Schmatz, J. and Urai, J.L., 2015. Nanoscale porosity analysis in geological materials. *Acta*  
748 *Stereologica*.
- 749 Kameda, A., Dvorkin, J., Keehm, Y., Nur, A. and Bosl, W., 2006. Permeability-porosity transforms from small  
750 sandstone fragments. *Geophysics*, 71(1), pp.N11-N19.
- 751 Karaborni, S., Smit, B., Heidug, W., Urai, J. and Van Oort, E., 1996. The swelling of clays: molecular simulations  
752 of the hydration of montmorillonite. *Science*, 271(5252), pp.1102-1104.



- 753 Klaver, J., Desbois, G., Littke, R. and Urai, J.L., 2015. BIB-SEM characterization of pore space morphology and  
754 distribution in postmature to overmature samples from the Haynesville and Bossier Shales. *Marine and petroleum*  
755 *Geology*, 59, pp.451-466.
- 756 Klaver, J., Desbois, G., Littke, R. and Urai, J.L., 2016. BIB-SEM pore characterization of mature and post mature  
757 Posidonia Shale samples from the Hils area, Germany. *International Journal of Coal Geology*, 158, pp.78-89.
- 758 Klaver, J., Desbois, G., Urai, J.L. and Littke, R., 2012. BIB-SEM study of the pore space morphology in early  
759 mature Posidonia Shale from the Hils area, Germany. *International Journal of Coal Geology*, 103, pp.12-25.
- 760 Klaver, J., Desbois, G., Urai, J.L. and Littke, R., 2012. BIB-SEM study of the pore space morphology in early  
761 mature Posidonia Shale from the Hils area, Germany. *International Journal of Coal Geology*, 103, pp.12-25.
- 762 Klaver, J., Hemes, S., Houben, M., Desbois, G., Radi, Z. and Urai, J.L., 2015. The connectivity of pore space in  
763 mudstones: insights from high-pressure Wood's metal injection, BIB-SEM imaging, and mercury intrusion  
764 porosimetry. *Geofluids*, 15(4), pp.577-591.
- 765 Klaver, J., Hemes, S., Houben, M., Desbois, G., Radi, Z. and Urai, J.L., 2015. The connectivity of pore space in  
766 mudstones: insights from high-pressure Wood's metal injection, BIB-SEM imaging, and mercury intrusion  
767 porosimetry. *Geofluids*, 15(4), pp.577-591.
- 768 Klinkenberg, M., Kaufhold, S., Dohrmann, R. and Siegesmund, S., 2009. Influence of carbonate microfabrics on  
769 the failure strength of claystones. *Engineering Geology*, 107(1-2), pp.42-54.
- 770 Kooi, H., 1997. Insufficiency of compaction disequilibrium as the sole cause of high pore fluid pressures in pre-  
771 Cenozoic sediments. *Basin Research*, 9(3), pp.227-241.
- 772 Kuila, U. and Prasad, M., 2013. Specific surface area and pore-size distribution in clays and shales. *Geophysical*  
773 *Prospecting*, 61(2-Rock Physics for Reservoir Exploration, Characterisation and Monitoring), pp.341-362.
- 774 Kuncoro, A.K., Cubas, N., Singh, S.C., Etchebes, M. and Tapponnier, P., 2015. Tsunamigenic potential due to  
775 frontal rupturing in the Sumatra locked zone. *Earth and Planetary Science Letters*, 432, pp.311-322.
- 776 Lahann, R., Huffman, A.R. and Bowers, G.L., 2002. Impact of smectite diagenesis on compaction modeling and  
777 compaction equilibrium. *MEMOIRS-AMERICAN ASSOCIATION OF PETROLEUM GEOLOGISTS*, pp.61-  
778 72.
- 779 Lambe, T.W., 1953, October. The structure of inorganic soil. In *Proceedings of the American Society of Civil*  
780 *Engineers* (Vol. 79, No. 10, pp. 1-49). ASCE.
- 781 Lambe, T.W., 1958. The structure of compacted clays. *Journal of the Soil Mechanics and Foundations*  
782 *Division*, 84(2), pp.1654-1.





- 783 Lander, R. H. and O. Walderhaug 1999. Predicting porosity through simulating sandstone compaction and quartz  
784 cementation. *American Association of Petroleum Geologists Bulletin* 83: 433-449.
- 785 Lander, R. H., R. H. Larese and L. M. Bonnell 2008. Toward more accurate quartz cement models: The importance  
786 of euhedral versus noneuhedral growth rates. *American Association Petroleum Geologists Bulletin* 92: 1537-1563.
- 787 Laurich, B., Urai, J.L. and Nussbaum, C., 2017. Microstructures and deformation mechanisms in Opalinus Clay:  
788 Insights from scaly clay from the Main Fault in the Mont Terri Rock Laboratory (CH). *Solid Earth*, 8(1), pp.27-  
789 44.
- 790 Laurich, B., Urai, J.L., Desbois, G., Vollmer, C. and Nussbaum, C., 2014. Microstructural evolution of an incipient  
791 fault zone in Opalinus Clay: Insights from an optical and electron microscopic study of ion-beam polished samples  
792 from the Main Fault in the Mt-Terri Underground Research Laboratory. *Journal of Structural Geology*, 67, pp.107-  
793 128.
- 794 Lay, T., Ammon, C.J., Kanamori, H., Yamazaki, Y., Cheung, K.F. and Hutko, A.R., 2011. The 25 October 2010  
795 Mentawai tsunami earthquake (Mw 7.8) and the tsunami hazard presented by shallow megathrust  
796 ruptures. *Geophysical Research Letters*, 38(6).
- 797 Lay, T., Kanamori, H., Ammon, C.J., Nettles, M., Ward, S.N., Aster, R.C., Beck, S.L., Bilek, S.L., Brudzinski,  
798 M.R., Butler, R. and DeShon, H.R., 2005. The great Sumatra-Andaman earthquake of 26 december  
799 2004. *science*, 308(5725), pp.1127-1133.
- 800 Lazar, O.R., Bohacs, K.M., Macquaker, J.H., Schieber, J. and Demko, T.M., 2015. Capturing key attributes of  
801 fine-grained sedimentary rocks in outcrops, cores, and thin sections: nomenclature and description  
802 guidelines. *Journal of Sedimentary Research*, 85(3), pp.230-246.
- 803 Li, Z. and J. Schieber 2018. Composite particles in mudstones: Examples from the Late Cretaceous Tununk shale  
804 member of the Mancos Shale Formation. *Journal of Sedimentary Research* 8812: 1319-1344. Lithic grains in shale
- 805 Li, Z., J. Schieber and P. K. Pedersen 2021. On the origin and significance of composite particles in mudstones;  
806 examples from the Cenomanian Dunvegan Formation. *Sedimentology* 682: 737-754. Lithic grains in shale
- 807 Logan, J.M. and Rauenzahn, K.A., 1987. Frictional dependence of gouge mixtures of quartz and montmorillonite  
808 on velocity, composition and fabric. *Tectonophysics*, 144(1-3), pp.87-108.
- 809 Lu, J., K. L. Milliken and R. M. Reed 2011. Diagenesis and sealing capacity of the Middle Tuscaloosa mudstone  
810 at the Cranfield CO<sub>2</sub> injection site, Mississippi, USA. *Environmental Geosciences* 3: 35-53.
- 811 Lundegard, P. D. 1992. Sandstone porosity loss--a 'big picture' view of the importance of compaction. *Journal of*  
812 *Sedimentary Petrology* 62: 250-260.



- 813 Lupini, J.F., Skinner, A.E. and Vaughan, P.R., 1981. The drained residual strength of cohesive  
814 soils. *Geotechnique*, 31(2), pp.181-213.
- 815 Mandelbrot, B.B., Pfeifer, P., Biham, O., Malcai, O., Lidar, D. and Avnir, D., 1998. Is nature  
816 fractal?. *Science*, 279(5352), pp.783-783.
- 817 March, A., 1932. *Mathematische Theorie der Regelung nach der Korngestalt bei affiner Deformation: Zeitschrift*  
818 *für Kristallographie*, v. 81.
- 819 McNeill, L.C. and Henstock, T.J., 2014. Forearc structure and morphology along the Sumatra-Andaman  
820 subduction zone. *Tectonics*, 33(2), pp.112-134.
- 821 McNeill, L.C., Dugan, B. and Petronotis, K.E., *The Expedition 362 Scientists (2017). Sumatra Subduction*  
822 *Zone. Proceedings of the International Ocean Discovery Program*, 362.
- 823 Meade, R.H., 1964. *Removal of water and rearrangement of particles during the compaction of clayey sediments.*  
824 *US Government Printing Office.*
- 825 Miller, S.A., 2013. The role of fluids in tectonic and earthquake processes. In *Advances in geophysics (Vol. 54,*  
826 *pp. 1-46). Elsevier.*
- 827 Milliken K. L. 2019. Compactional and mass-balance constraints inferred from the volume of quartz cementation  
828 in mudrocks. *Mudstone Diagenesis: New Research Perspectives for Shale Hydrocarbon Reservoirs, Seals, and*  
829 *Source Rocks. AAPG. 120: 33-48.*
- 830 Milliken, K. L. 2014. A compositional classification for grain assemblages in fine-grained sediments and  
831 sedimentary rocks. *Journal of Sedimentary Research* 84: 1185-1199.
- 832 Milliken, K. L. and M. E. Curtis 2016. Imaging pores in sedimentary rocks: Foundation of porosity prediction.  
833 *Marine and Petroleum Geology* 73: 590-608.
- 834 Milliken, K. L. and R. J. Day-Stirrat 2013. Cementation in mudrocks: Brief review with examples from cratonic  
835 basin mudrocks. *Memoir. J.-Y. Chatellier. Tulsa, Oklahoma, USA, AAPG: in press.*
- 836 Milliken, K. L. and T. Olson 2017. Silica diagenesis, porosity evolution, and mechanical behavior in siliceous  
837 mudstones, Mowry Shale Cretaceous, Rocky Mountains, U.S.A. *Journal of Sedimentary Research* 87: 366-387.
- 838 Milliken, K. L., M. Rudnicki, D. N. Awwiller and T. Zhang 2013. Organic matter-hosted pore system, Marcellus  
839 Formation Devonian, Pennsylvania, USA. *AAPG Bulletin* 97: 177-200.
- 840 Milliken, K. L., W. L. Esch, R. M. Reed and T. Zhang 2012. Grain assemblages and strong diagenetic overprinting  
841 in siliceous mudrocks, Barnett Shale Mississippian, Fort Worth Basin, Texas, U.S.A. *AAPG Bulletin* 96: 1553-  
842 1578.



- 843 Milliken, K., and Olson, T., 2016, Amorphous and crystalline solids as artifacts in SEM images, in Olson, T.,  
844 Imaging Unconventional Reservoir Pore Systems: AAPG Memoir, v. 112, p. 1-8,  
845 <http://doi.org/10.1306/13592013M112252>.
- 846 Milliken, K.L. and Hayman, N.W., 2019. Mudrock components and the genesis of bulk rock properties: review of  
847 current advances and challenges. *Shale: Subsurface Science and Engineering*, pp.1-25.
- 848 Mitchell, J.K., 1956. The fabric of natural clays and its relation to engineering properties. In Highway Research  
849 Board Proceedings (Vol. 35).
- 850 Moeremans, R., Singh, S.C., Mukti, M., McArdle, J. and Johansen, K., 2014. Seismic images of structural  
851 variations along the deformation front of the Andaman–Sumatra subduction zone: implications for rupture  
852 propagation and tsunamigenesis. *Earth and Planetary Science Letters*, 386, pp.75-85.
- 853 Moeremans, R.E. and Singh, S.C., 2014. Seismic evidence of continental margin influence on the NinetyEast  
854 Ridge in the Bay of Bengal. *Geophysical Research Letters*, 41(20), pp.7143-7150.
- 855 Moeremans, R.E. and Singh, S.C., 2015. Fore-arc basin deformation in the Andaman-Nicobar segment of the  
856 Sumatra-Andaman subduction zone: Insight from high-resolution seismic reflection data. *Tectonics*, 34(8),  
857 pp.1736-1750.
- 858 Mondol, N.H., Bjørlykke, K., Jahren, J. and Høeg, K., 2007. Experimental mechanical compaction of clay mineral  
859 aggregates—Changes in physical properties of mudstones during burial. *Marine and petroleum geology*, 24(5),  
860 pp.289-311.
- 861 Moon, C.F., 1972. The microstructure of clay sediments. *Earth-Science Reviews*, 8(3), pp.303-321.
- 862 Moore, D.E. and Lockner, D.A., 2004. Crystallographic controls on the frictional behavior of dry and water-  
863 saturated sheet structure minerals. *Journal of Geophysical Research: Solid Earth*, 109(B3).
- 864 Moore, D. M. and R. C. Reynolds, Jr. (1989). X-ray diffraction and the identification and analysis of clay minerals.  
865 United States, Oxford Univ. Press : New York, NY, 332 p. Morgenstern, N.R. and Tchalenko, J.S., 1967.  
866 Microscopic structures in kaolin subjected to direct shear. *Geotechnique*, 17(4), pp.309-328.
- 867 Morgenstern, N.R. and Tchalenko, J.S., 1967. Microscopic structures in kaolin subjected to direct  
868 shear. *Geotechnique*, 17(4), pp.309-328.
- 869 Nakano, R., 1967. On weathering and change of properties of tertiary mudstone related to landslide. *Soils and*  
870 *Foundations*, 7(1), pp.1-14.
- 871 Neagu, R.C., Cartwright, J. and Davies, R., 2010. Measurement of diagenetic compaction strain from quantitative  
872 analysis of fault plane dip. *Journal of Structural Geology*, 32(5), pp.641-655.



- 873 Oertel, G. and Curtis, C.D., 1972. Clay-ironstone concretion preserving fabrics due to progressive  
874 compaction. *Geological Society of America Bulletin*, 83(9), pp.2597-2606.
- 875 Paxton, S. T., J. O. Szabo, J. M. Adjukiewicz and R. E. Klimentidis 2002. Construction of an intergranular volume  
876 compaction curve for evaluating and predicting compaction and porosity loss in rigid-grain sandstone reservoirs.  
877 *American Association of Petroleum Geologists Bulletin* 86: 2047-2067.
- 878 Pickering, K. T., H. Poudroux, L. C. McNeill, J. Backman, F. Chemale, S. Kutterolf, K. L. Milliken, H.  
879 Mukoyoshi, T. J. Henstock, D. E. Stevens, C. Parnell and B. Dugan, 2020. Sedimentology, stratigraphy and  
880 architecture of the Nicobar Fan (BengalNicobar Fan System), Indian Ocean: Results from International Ocean  
881 Discovery Program Expedition 362. *Sedimentology* 67(5): 2248-2281.
- 882 Philipp, T., Amann-Hildenbrand, A., Laurich, B., Desbois, G., Littke, R. and Urai, J.L., 2017. The effect of  
883 microstructural heterogeneity on pore size distribution and permeability in Opalinus Clay (Mont Terri,  
884 Switzerland): insights from an integrated study of laboratory fluid flow and pore morphology from BIB-SEM  
885 images. *Geological Society, London, Special Publications*, 454(1), pp.85-106.
- 886 Pommer, M. E. and K. L. Milliken 2015. Pore types and pore-size distributions across thermal maturity, Eagle  
887 Ford Formation, South Texas. *AAPG Bulletin* 99: 1713-1744.
- 888 Porter, J.R., Knipe, R.J., Fisher, Q.J., Farmer, A.B., Allin, N.S., Jones, L.S., Palfrey, A.J., Garrett, S.W. and Lewis,  
889 G., 2000. Deformation processes in the Britannia Field, UKCS. *Petroleum Geoscience*, 6(3), pp.241-254.
- 890 Prawirodirdjo, L., Bocl, Y., McCaffrey, R., Genrich, J., Calais, E., Stevens, C., Puntodewo, S.S.O., Subarya, C.,  
891 Rais, J., Zwick, P. and Fauzi, R.M., 1997. Geodetic observations of interseismic strain segmentation at the Sumatra  
892 subduction zone. *Geophysical research letters*, 24(21), pp.2601-2604.
- 893 Proctor, B., Lockner, D.A., Kilgore, B.D., Mitchell, T.M. and Beeler, N.M., 2020. Direct evidence for fluid  
894 pressure, dilatancy, and compaction affecting slip in isolated faults. *Geophysical Research Letters*, 47(16),  
895 p.e2019GL086767.
- 896 Rabinowitz, H.S., Savage, H.M., Skarbek, R.M., Ikari, M.J., Carpenter, B.M. and Colletini, C., 2018. Frictional  
897 behavior of input sediments to the Hikurangi Trench, New Zealand. *Geochemistry, Geophysics,  
898 Geosystems*, 19(9), pp.2973-2990.
- 899 Rosenberger, K., Underwood, M.B., Vrolijk, P. and Haines, S., 2020. Data report: clay mineral assemblages in  
900 hemipelagic sediments entering the Sumatra subduction zone, IODP Sites U1480 and U1481, Expedition  
901 362. *Expedition*, 362, p.1.
- 902 Rubey, W.W. and King Hubbert, M., 1959. Role of fluid pressure in mechanics of overthrust faulting: II.  
903 Overthrust belt in geosynclinal area of western Wyoming in light of fluid-pressure hypothesis. *Geological Society  
904 of America Bulletin*, 70(2), pp.167-206.



- 905 Rutter, E.H., Maddock, R.H., Hall, S.H. and White, S.H., 1986. Comparative microstructures of natural and  
906 experimentally produced clay-bearing fault gouges. *Pure and applied geophysics*, 124(1), pp.3-30.
- 907 Rybacki, E., Morales, L.F.G., Naumann, M. and Dresen, G., 2014. Strain localization during high temperature  
908 creep of marble: The effect of inclusions. *Tectonophysics*, 634, pp.182-197.
- 909 Saffer, D.M. and Bekins, B.A., 2006. An evaluation of factors influencing pore pressure in accretionary complexes:  
910 Implications for taper angle and wedge mechanics. *Journal of Geophysical Research: Solid Earth*, 111(B4).
- 911 Saito, S. and Goldberg, D., 2001. Compaction and dewatering processes of the oceanic sediments in the Costa  
912 Rica and Barbados subduction zones: estimates from in situ physical property measurements. *Earth and Planetary  
913 Science Letters*, 191(3-4), pp.283-293.
- 914 Salman, R., Lindsey, E.O., Feng, L., Bradley, K., Wei, S., Wang, T., Daryono, M.R. and Hill, E.M., 2020.  
915 Structural controls on rupture extent of recent Sumatran Fault Zone earthquakes, Indonesia. *Journal of Geophysical  
916 Research: Solid Earth*, 125(2), p.e2019JB018101.
- 917 Samsudin, M.S.F., Ariff, Z.M. and Ariffin, A., 2017, April. Deformation behavior of open-cell dry natural rubber  
918 foam: Effect of different concentration of blowing agent and compression strain rate. In *AIP Conference  
919 Proceedings* (Vol. 1835, No. 1, p. 020007). AIP Publishing LLC.
- 920 Schieber, J. 2016. Experimental testing of the transport-durability of shale lithics and its implications for  
921 interpreting the rock record. *Sedimentary Geology* 331: 162-169. Lithic grains in shale
- 922 Schieber, J., J. Southard and K. Thaisen 2007. Accretion of mudstone beds from migrating floccule ripples. *Science*  
923 3185857: 1760-1763. Floccules in the range of sand-size.
- 924 Schmatz, J., Klaver, J., Jiang, M. and Urai, J.L., 2017. Nanoscale morphology of brine/oil/mineral contacts in  
925 connected pores of carbonate reservoirs: Insights on wettability from Cryo-BIB-SEM. *SPE Journal*, 22(05),  
926 pp.1374-1384.
- 927 Schneider, J., Flemings, P.B., Day-Stirrat, R.J. and Germaine, J.T., 2011. Insights into pore-scale controls on  
928 mudstone permeability through re-sedimentation experiments. *Geology*, 39(11), pp.1011-1014.
- 929 Singh, S.C., Hananto, N., Mukti, M., Robinson, D.P., Das, S., Chauhan, A., Carton, H., Gratacos, B., Midnet, S.,  
930 Djajadihardja, Y. and Harjono, H., 2011. Aseismic zone and earthquake segmentation associated with a deep  
931 subducted seamount in Sumatra. *Nature Geoscience*, 4(5), pp.308-311.
- 932 Sintubin, M., 1994. Clay fabrics in relation to the burial history of shales. *Sedimentology*, 41(6), pp.1161-1169.
- 933 Terzaghi, K., 1925. Principles of soil mechanics: V — physical differences between sand and clay. *Engineering  
934 News Record* 96, 912–915.



- 935 Terzaghi, K., Peck, R.B., 1948. Soil Mechanics In Engineering Practice. John Wiley and Sons, New York.
- 936 Torres, M. E. and K. Milliken (2019). Linked carbonate cementation and silicate dissolution in the sediments of  
937 the Bengal-Nicobar Fan, inputs to the Sumatra subduction zone. prresAmerican Geophysical Union Fall Meeting  
938 2019.
- 939 Tunega, D. and Zaoui, A., 2020. Mechanical and bonding behaviors behind the bending mechanism of kaolinite  
940 clay layers. The Journal of Physical Chemistry C, 124(13), pp.7432-7440.
- 941 Ukar, E. and Cloos, M., 2019. Cataclastic deformation and metasomatism in the subduction zone of mafic blocks-  
942 in-mélange, San Simeon, California. Lithos, 346, p.105116.
- 943 Van Olphen, H., 1964. Internal mutual flocculation in clay suspensions. Journal of Colloid Science, 19(4), pp.313-  
944 322.
- 945 Vasseur, G., Djeran-Maigre, I., Grunberger, D., Rousset, G., Tessier, D. and Velde, B., 1995. Evolution of  
946 structural and physical parameters of clays during experimental compaction. Marine and petroleum  
947 geology, 12(8), pp.941-954.
- 948 Velde, B. 1996. Compaction trends of clay-rich deep sea sediments. Marine Geology 133(3-4): 193-201.
- 949 Voltolini, M., Wenk, H.R., Mondol, N.H., Bjørlykke, K. and Jahren, J., 2009. Anisotropy of experimentally  
950 compressed kaolinite-illite-quartz mixtures. Geophysics, 74(1), pp.D13-D23.
- 951 Vrolijk, P., 1990. On the mechanical role of smectite in subduction zones. Geology, 18(8), pp.703-707.
- 952 Walker, K.T., Ishii, M. and Shearer, P.M., 2005. Rupture details of the 28 March 2005 Sumatra Mw 8.6 earthquake  
953 imaged with teleseismic P waves. Geophysical Research Letters, 32(24).
- 954 Wang, X., Jiang, Z., Jiang, S., Chang, J., Zhu, L., Li, X. and Li, J., 2019. Full-scale pore structure and fractal  
955 dimension of the Longmaxi shale from the Southern Sichuan Basin: Investigations using FE-SEM, gas adsorption  
956 and mercury intrusion porosimetry. Minerals, 9(9), p.543.
- 957 Wei, L.I., Jun, X.I.E., GAO, X.H., ZHANG, L.H. and Fang, Y.U., 2008. Characteristics of Jurassic mudstone  
958 overpressure and its control on oil and gas accumulation in Turpan Depression. Petroleum Exploration and  
959 Development, 35(1), pp.28-33.
- 960 Wenk, H.R., Voltolini, M., Kern, H., Popp, T. and Mazurek, M., 2008. Anisotropy in shale from Mont Terri. The  
961 Leading Edge, 27(6), pp.742-748.
- 962 Worden, R.H., Charpentier, D., Fisher, Q.J. and Aplin, A.C., 2005. Fabric development and the smectite to illite  
963 transition in Upper Cretaceous mudstones from the North Sea: an image analysis approach. Geological Society,  
964 London, Special Publications, 249(1), pp.103-114.



965 Yagiz, S., 2001. Overview of classification and engineering properties of shales for design considerations.  
966 In *Construction and Materials Issues 2001* (pp. 156-165).

967 Yawar, Z. and J. Schieber 2017. On the origin of silt laminae in laminated shales. *Sedimentary Geology* 360: 22-  
968 34. Shows that coarse silt does segregates from clay in transport but fine silt is part of silt-clay floccules---hence  
969 floccules are bigger than fine silt size around 20 microns.

970 Yong, R.N. and Sheeran, D.E., 1973. Fabric unit interaction and soil behaviour. In *Proceedings International*  
971 *Symposium on Soil Structure*.

972 Zakaria, Z., Mohamad Ariff, Z. and Abu Bakar, A., 2018. Monitoring deformation mechanism of foam cells in  
973 polyethylene foams via optical microscopy: Effect of density and microstructure. *Journal of Cellular*  
974 *Plastics*, 54(6), pp.957-976.

975 Zhou, J., Shrotriya, P. and Soboyejo, W.O., 2004. Mechanisms and mechanics of compressive deformation in  
976 open-cell Al foams. *Mechanics of Materials*, 36(8), pp.781-797.

977

978

979

980

981

982

983

984

985

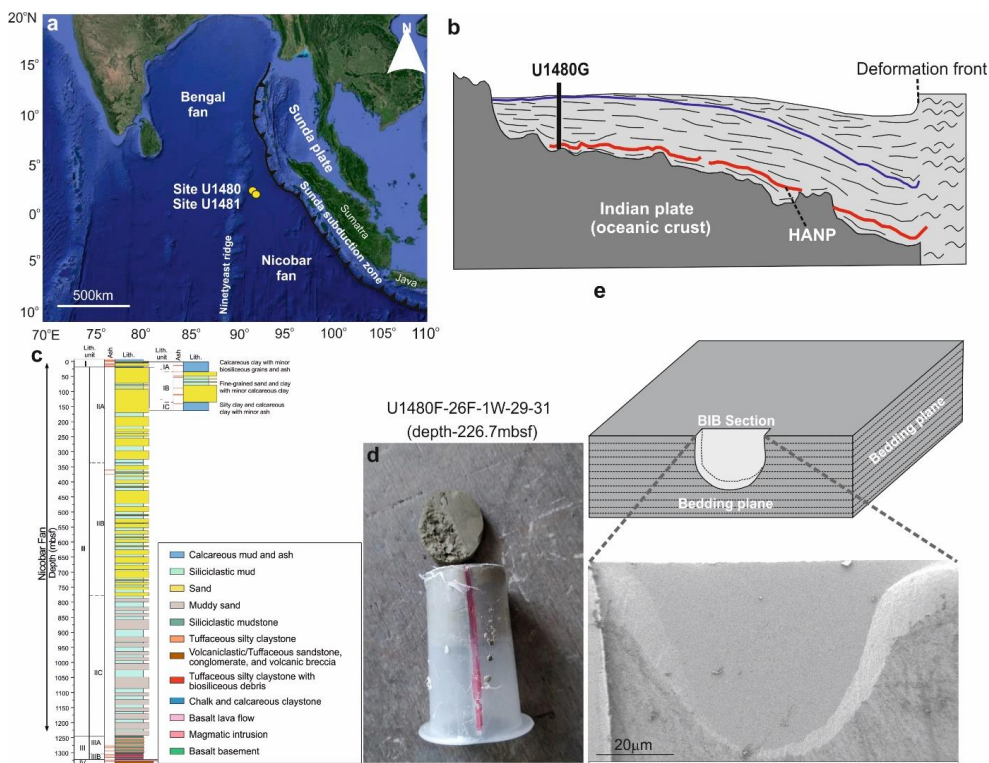
986

987

988

989

990



991

992 **Fig.1:** (a) Geological map of Sumatra subduction zone and location of U1480 and U1481 drilling sites (created  
 993 from © Google Maps). (b) Location of drilling site U1480 in sectional view (adapted from seismic profile after  
 994 Hüpers et al., 2017). (c) Lithostratigraphic units encountered at Site U1480 (adapted after McNeill et al., 2017).  
 995 (d) Representative tube sample received from IODP repository, Japan. Red-colored line on tube surface represents  
 996 notch used to denote orientation of samples collected from drill core. (e) Representative BIB cross-section polished  
 997 perpendicular to bedding planes.

998

999

1000

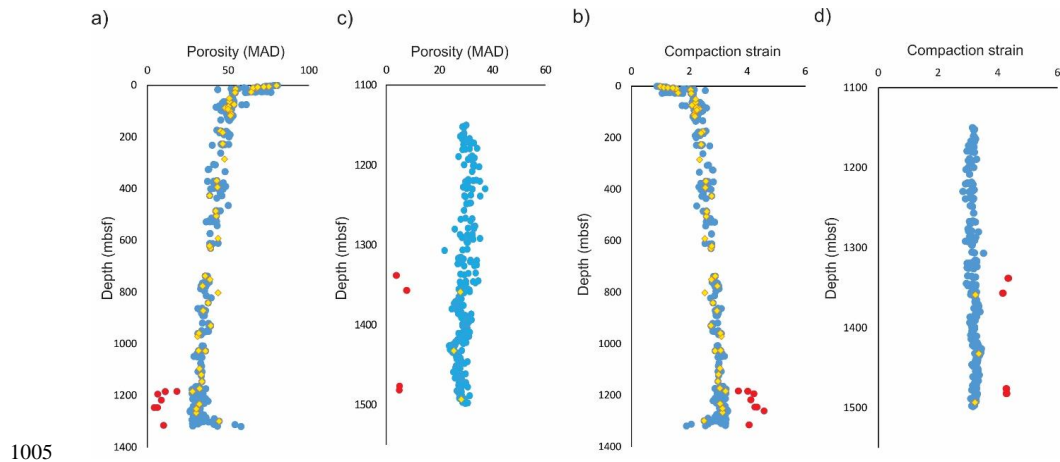
1001

1002

1003

1004





1005

1006 **Fig.2:** (a) and (b) Shipboard MAD (Moisture and density) porosity vs depth data for mudstone samples recovered  
1007 from Sites U1480 and U1481; (c) and (d) Cross-plot diagrams for estimated compaction strain vs depth  
1008 corresponding to samples recovered from Sites U1480 and U1481. Yellow-colored symbols in (a), (b), (c), and (d)  
1009 show 55 mud samples analyzed at RWTH-Aachen and BEG, Austin. Red-colored points are cemented (concretion)  
1010 samples.

1011

1012

1013

1014

1015

1016

1017

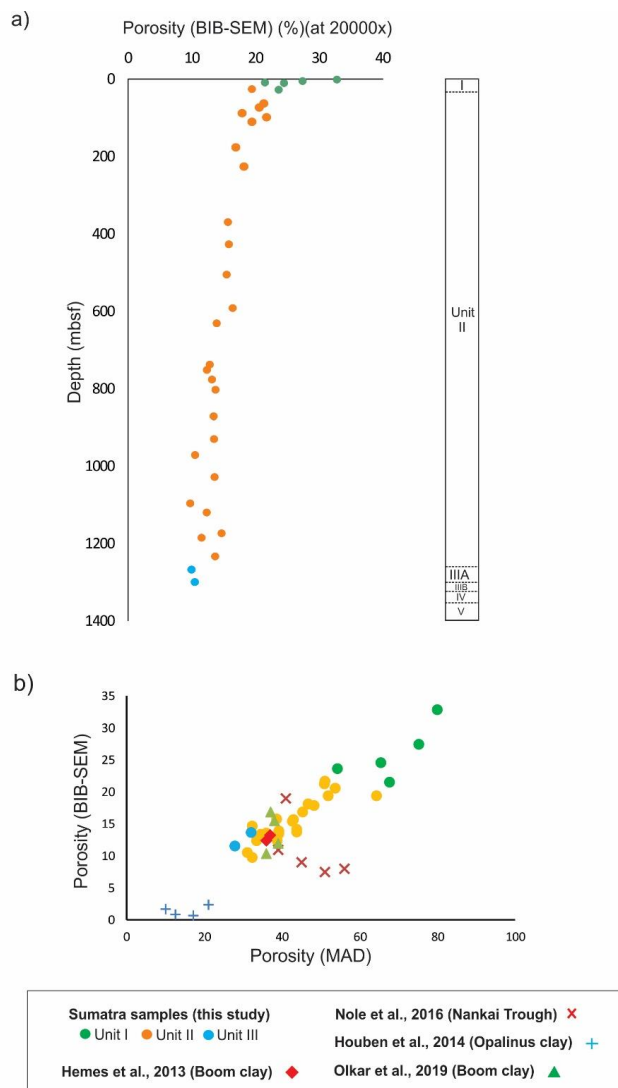
1018

1019

1020

1021

1022



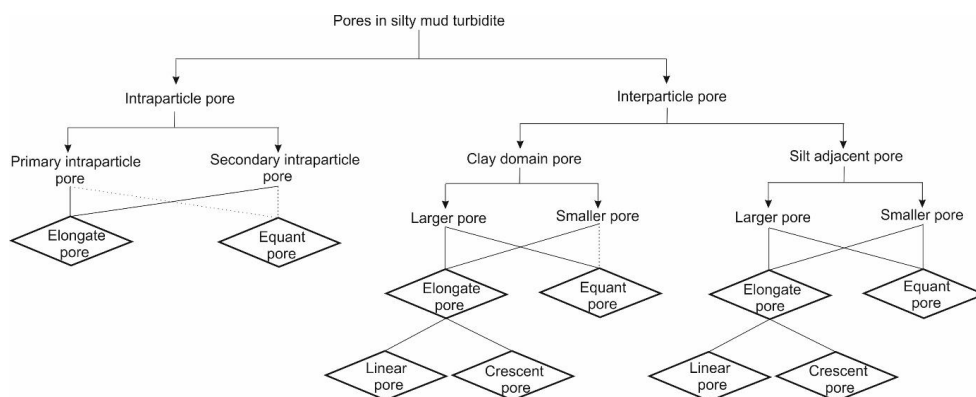
1023

1024 **Fig.3:** Porosity data for Units I (green dots), II (orange dots), and IIIA (blue dots). (a) BIB-SEM - depth plot. (b)  
1025 BIB-SEM porosity vs MAD porosity. Note: linear relationship that intersects origin. The data estimated by Hemes  
1026 et al., 2013; Houben et al., 2014; Olkar et al., 2019 also follow similar trend. However, the data estimated by Nole  
1027 et al., 2016 is deviated from the general trend.

1028



1029



1030

1031

1032 **Fig.4:** Classification scheme adopted to demonstrate pore reduction mechanics with increasing compactional  
1033 strain. Dashed lines indicate rare pore types.

1034

1035

1036

1037

1038

1039

1040

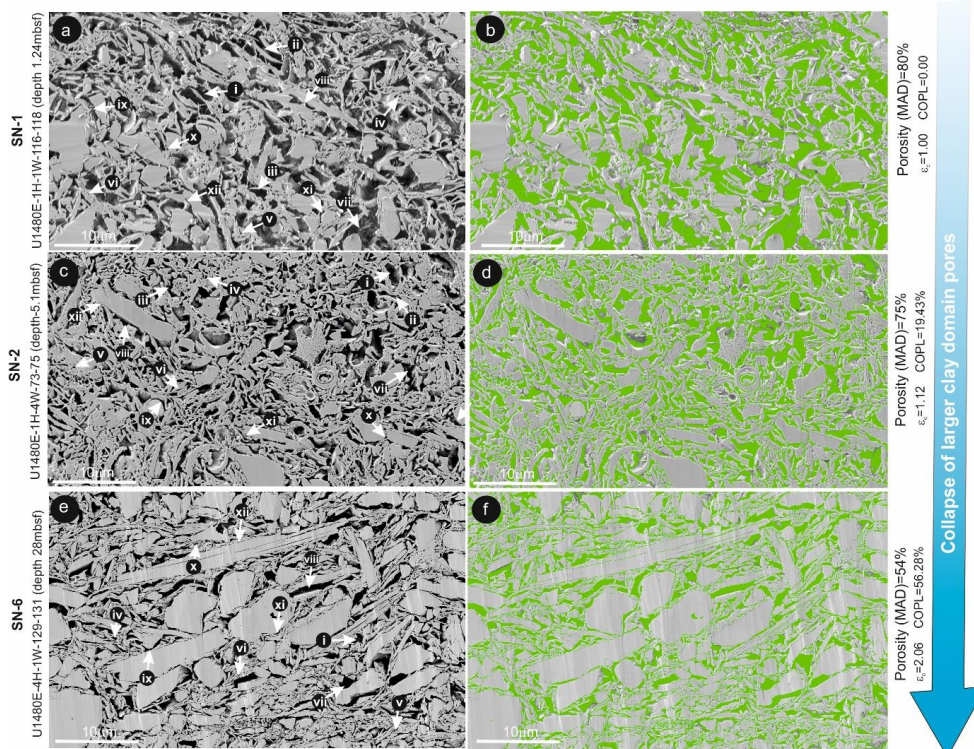
1041

1042

1043

1044

1045



1046

1047 **Fig.5:** Microstructural overview (BIB-SEM) of samples SN-1 (a and b), SN-2 (c and d), and SN-6 (e and f). Green  
 1048 color represents segmented pores of the corresponding microstructure of sample. i = Equant large clay domain  
 1049 pores, ii = elongated large clay domain pores, iii = Crescent-shaped large clay domain pores, iv = equant small  
 1050 clay domain pores, v = Crescent-shaped small clay domain pores, vi = elongated small clay domain pores, vii =  
 1051 Equant large silt-adjacent pores, viii = elongated large silt-adjacent pores, ix = Crescent-shaped large silt-adjacent  
 1052 pores, x = equant small silt-adjacent pores, xi = Crescent-shaped small silt-adjacent pores, xii = elongated small  
 1053 silt-adjacent pores.

1054

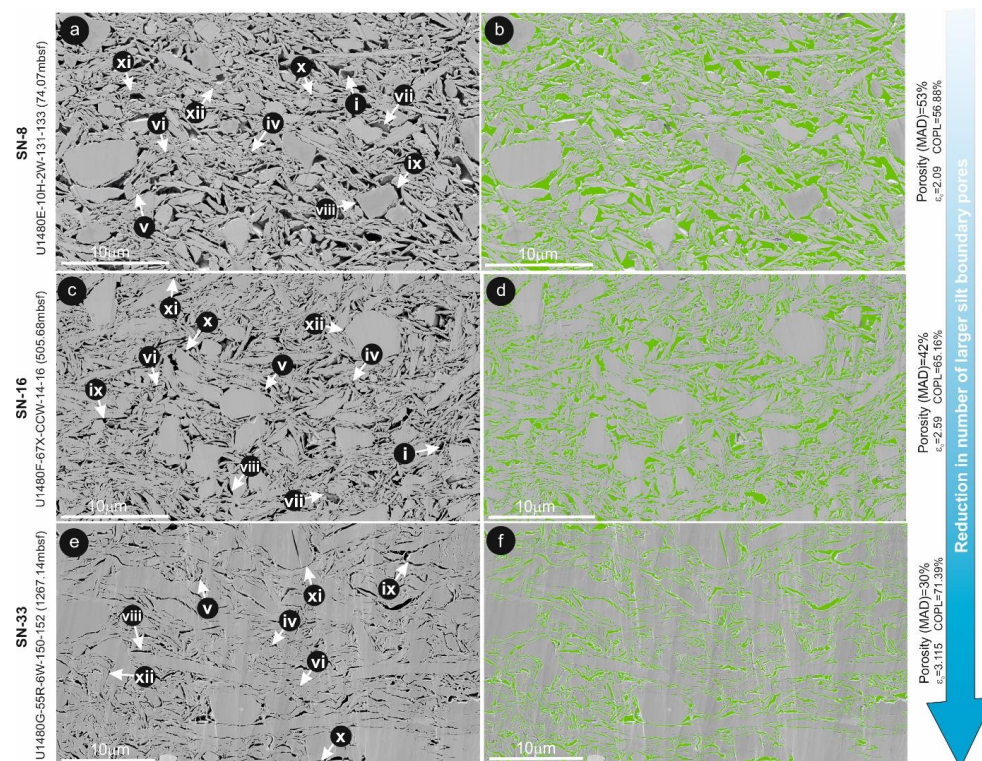
1055

1056

1057

1058

1059



1060

1061 **Fig.6:** Microstructural overview (BIB-SEM) of samples SN-8 (a and b), SN-16 (c and d), and SN-32 (e and f).  
 1062 Green color represents segmented pores of the corresponding microstructure of sample. i = Equant large clay  
 1063 domain pores, ii = elongated large clay domain pores, iii = Crescent-shaped large clay domain pores, iv = equant  
 1064 small clay domain pores, v = Crescent-shaped small clay domain pores, vi = elongated small clay domain pores,  
 1065 vii = Equant large silt-adjacent pores, viii = elongated large silt-adjacent pores, ix = Crescent-shaped large silt-  
 1066 adjacent pores, x = equant small silt-adjacent pores, xi = Crescent-shaped small silt-adjacent pores, xii = elongated  
 1067 small silt-adjacent pores.

1068

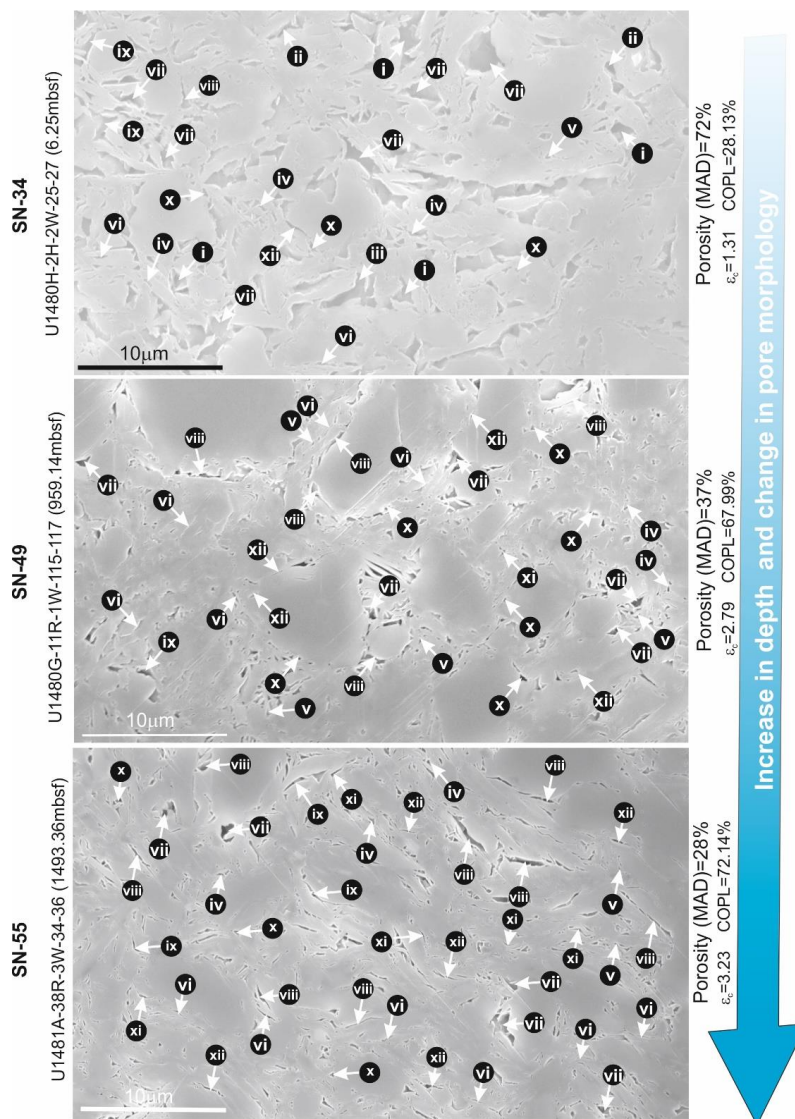
1069

1070

1071

1072

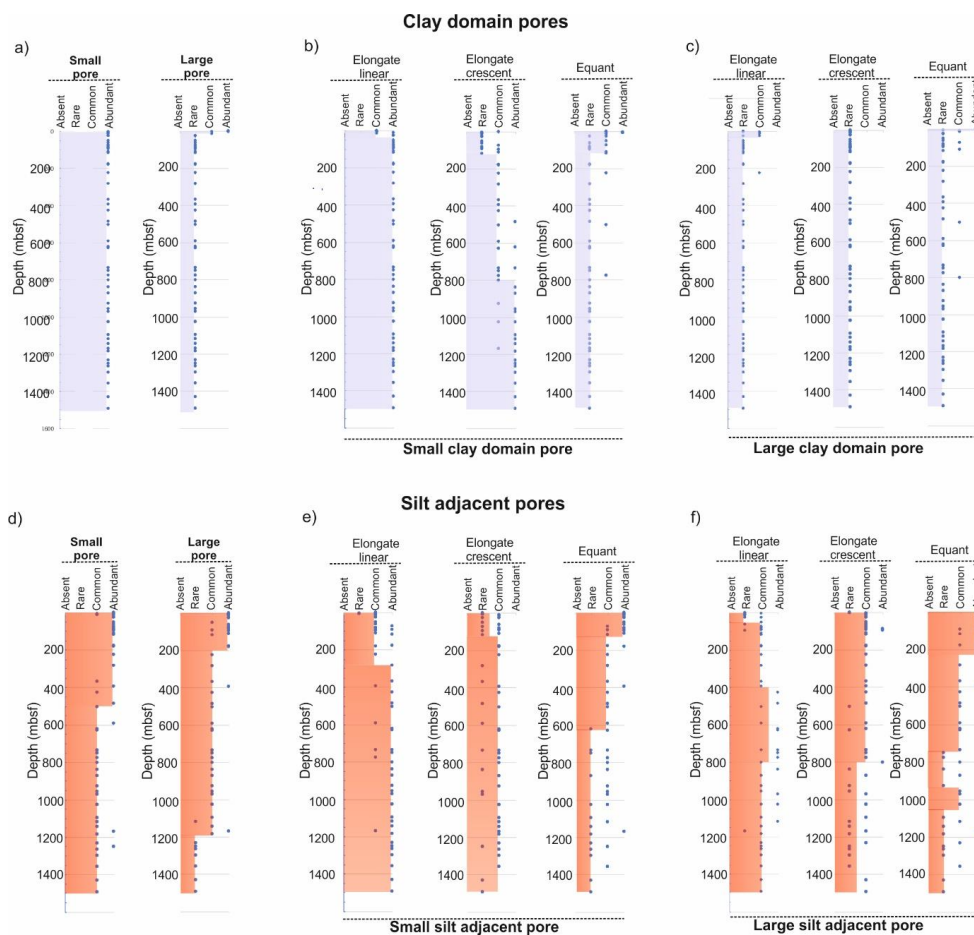
1073



1074

1075 **Fig.7:** Microstructural overview (Field Emission SEM) of samples SN-34, SN-49, and SN-55. i = Equant large  
 1076 clay domain pores, ii = elongated large clay domain pores, iii = Crescent-shaped large clay domain pores, iv =  
 1077 equant small clay domain pores, v = Crescent-shaped small clay domain pores, vi = elongated small clay domain  
 1078 pores, vii = Equant large silt-adjacent pores, viii = elongated large silt-adjacent pores, ix = Crescent-shaped large  
 1079 silt-adjacent pores, x = equant small silt-adjacent pores, xi = Crescent-shaped small silt-adjacent pores, xii =  
 1080 elongated small silt-adjacent pores.

1081



1082

1083 **Fig.8:** Pore type summary for clay domain (a-c) and silt-adjacent (d-f) pore types. (a) abundance of small and large  
 1084 clay domain pores; (b) and (c) depth progression of small and large clay domain pore morphologies; (d) abundance  
 1085 of small and large silt-adjacent pores; (e) and (f) depth progression of small and large clay domain pore  
 1086 morphologies. See text for abundance category definitions.

1087

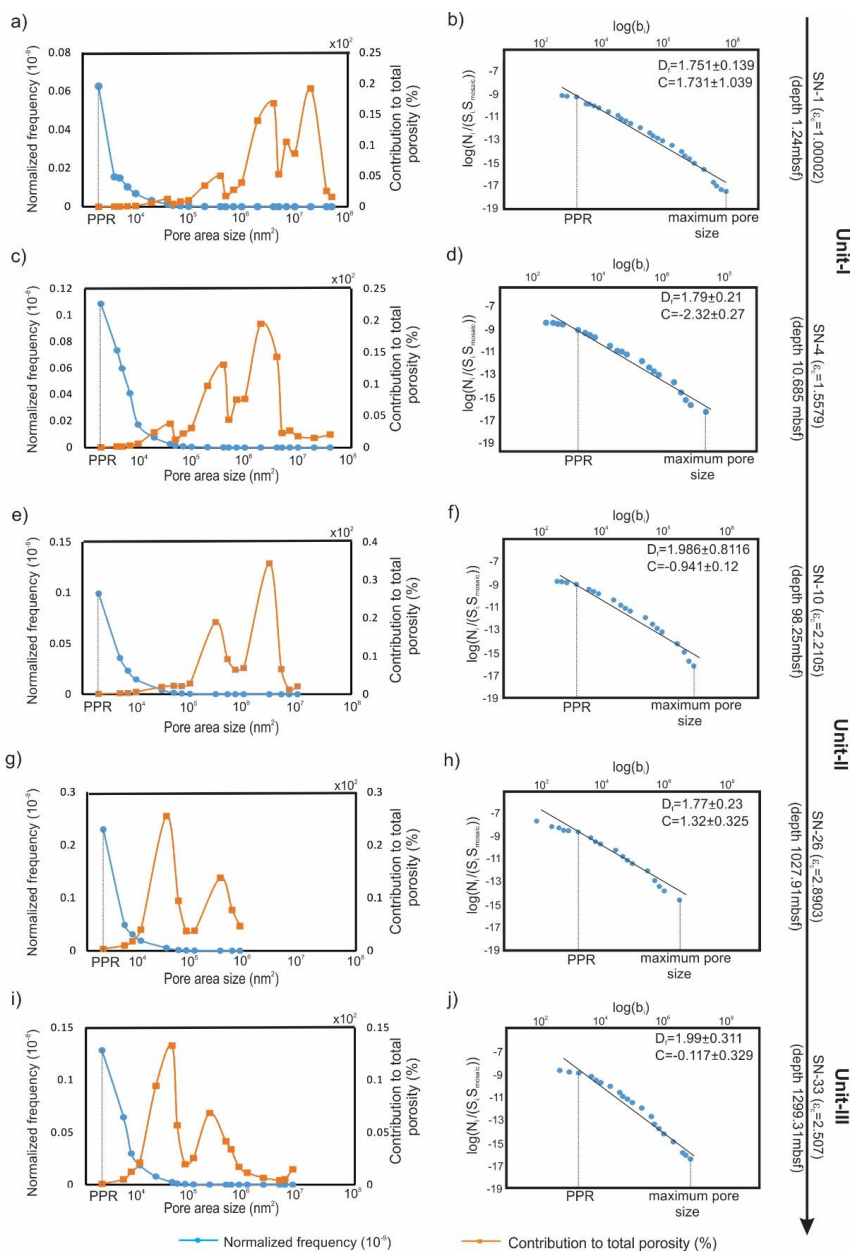
1088

1089

1090

1091

1092

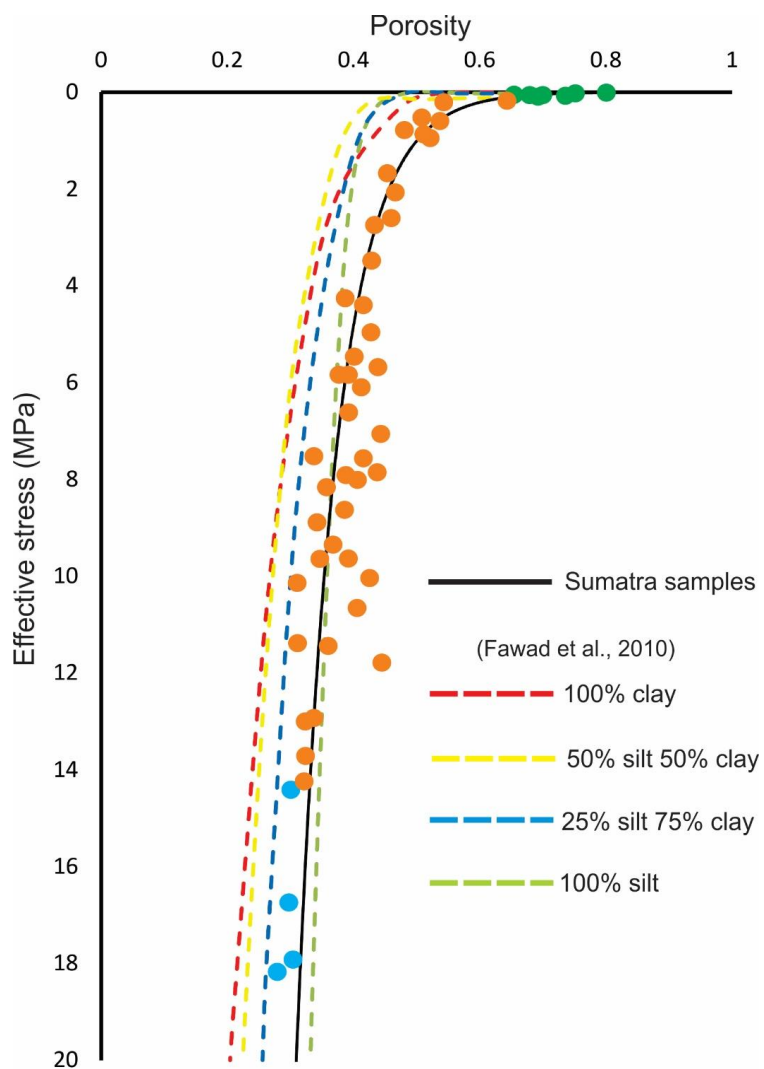


1093

1094 **Fig.9:** Pore size distribution defined by pore area. Left column: normalized frequency (blue) and contribution to  
 1095 total porosity (orange). Right column: pore size-frequency log-log distribution. Power-law between PPR and  
 1096 maximum pore size interpreted as black line with corresponding regression parameters. Sample number, depth,  
 1097 and compactional strain defined along right side of diagram

1098





1099

1100 **Fig.10:** Effective stress vs porosity for experimental mixtures of clay and silt (dashed lines; Fawad et al., 2010)  
1101 compared with Sumatra data (Unit 1 = green; Unit II = orange; Unit III = blue). Solid black solid line is a best-  
1102 fit data regression for Sumatra samples.

1103

1104

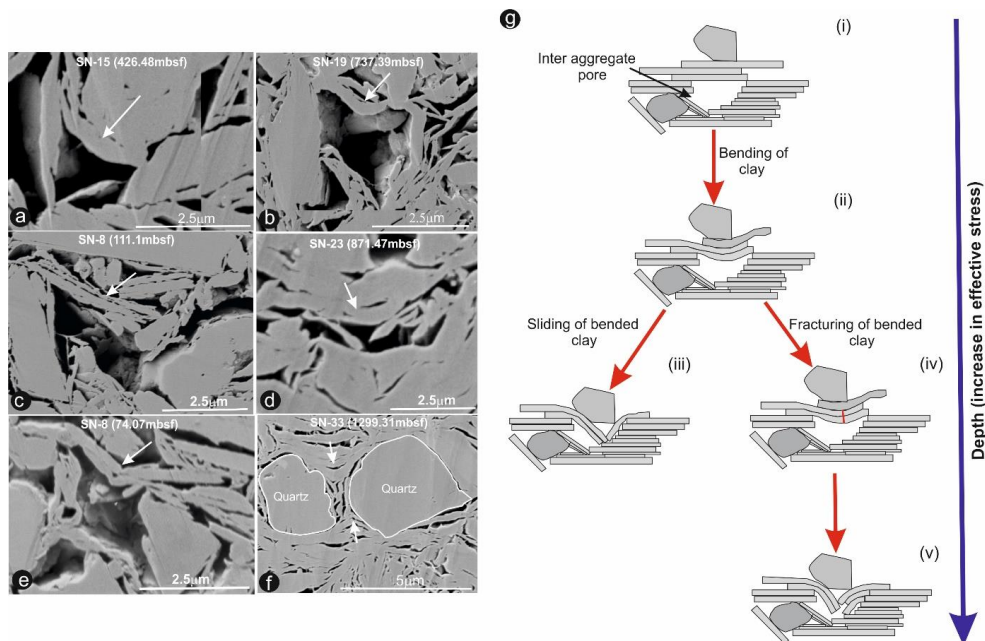
1105

1106



1107

1108



1109

1110 **Fig.11:** a-f: examples of bent clay particle on top of silt-adjacent larger pores; sample ID and depth labelled on  
1111 photos. (g) Micromechanical model for collapse of large silt-adjacent pores.

1112

1113

1114

1115

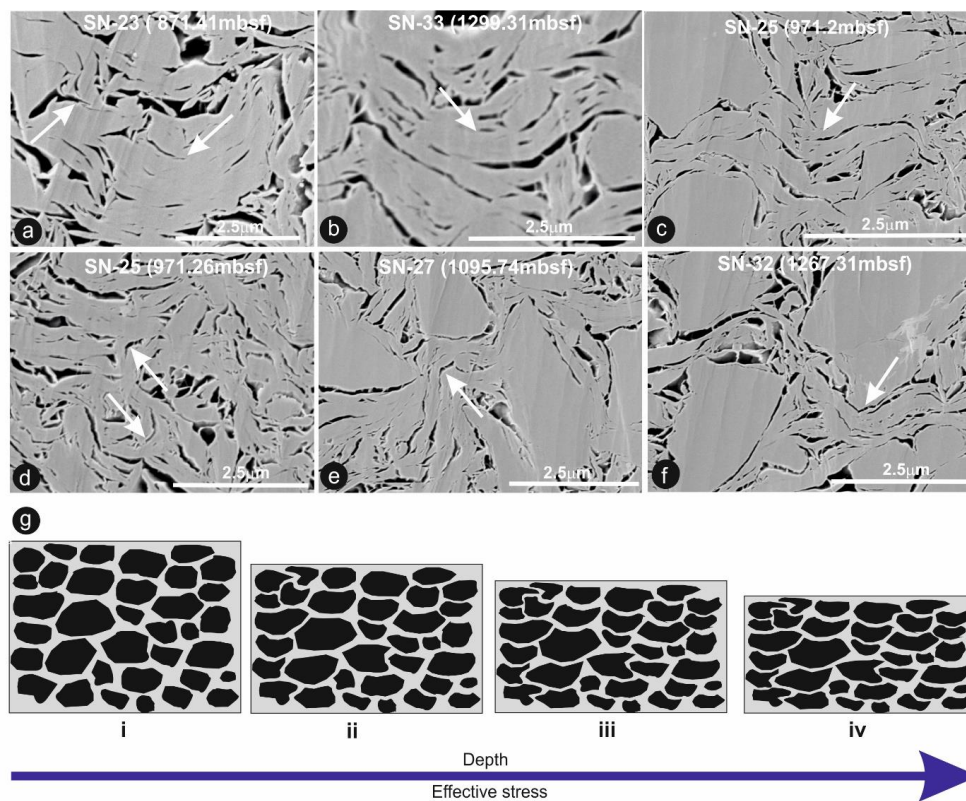
1116

1117

1118

1119

1120



1121

1122 **Fig.12:** a-f: examples of clay aggregate bending (white and black arrows). (g) Conceptual diagram tracing  
1123 porosity reduction and increase in preferred alignment of the long axes of pores by bending of clay perpendicular  
1124 to applied vertical stress.

1125

1126

1127

1128

1129

1130

1131

1132



1133 Table 1: Clay mineralogy in subunits of the Sumatra succession

1134	<b>Units</b>	<b>Smectite (%)</b>	<b>Illite (%)</b>
1135	Unit-I	33	49
1136	Unit-II	17	59
1137	Unit-III A	73	19

1139

1140

1141

1142

1143

1144

1145

1146

1147

1148

1149

1150

1151

1152

1153

1154



**Table 2:** Summary of pore morphology evolution with depth. Abundant = >25% pores, common = 2%-25% pores, rare = 0-2% pores, absent = not observed.

Depth (mbsf)	Sample no	Clay domain pores					Silt adjacent pores						
		Small pores (<5x10 <sup>5</sup> nm <sup>2</sup> )	Larger pores (>5x10 <sup>5</sup> nm <sup>2</sup> )	Small pore			Larger pore						
		Elongate linear	Elongate crescent	Equant	Elongate linear	Elongate crescent	Equant	Elongate linear	Elongate crescent	Equant	Elongate linear	Elongate crescent	Equant
1.24	SN-1	Abundant	Abundant	Rare	Rare	Rare	Abundant	Common	Common	Abundant	Rare	Rare	Abundant
5.10	SN-2	Abundant	Rare	Common	Rare	Rare	Abundant	Common	Common	Abundant	Common	Common	Abundant
6.25	SN-34	Abundant	Abundant	Common	Rare	Rare	Abundant	Common	Common	Abundant	Rare	Common	Abundant
7.21	SN-35	Abundant	Abundant	Common	Rare	Rare	Abundant	Common	Common	Abundant	Rare	Common	Abundant
9.18	SN-3	Abundant	Abundant	Common	Rare	Rare	Abundant	Common	Common	Abundant	Rare	Common	Abundant
10.69	SN-4	Abundant	Abundant	Rare	Rare	Rare	Common	Common	Common	Abundant	Rare	Common	Abundant
14.28	SN-36	Abundant	Abundant	Rare	Rare	Rare	Abundant	Common	Common	Abundant	Rare	Common	Abundant
26.05	SN-5	Abundant	Abundant	Rare	Rare	Rare	Abundant	Common	Common	Abundant	Rare	Common	Abundant
28.00	SN-6	Abundant	Abundant	Common	Rare	Rare	Abundant	Common	Common	Abundant	Common	Common	Abundant
28.12	SN-37	Abundant	Abundant	Common	Rare	Rare	Abundant	Common	Common	Abundant	Common	Common	Abundant
50.82	SN-38	Abundant	Abundant	Common	Rare	Rare	Abundant	Common	Common	Abundant	Common	Common	Abundant
63.24	SN-7	Abundant	Abundant	Common	Rare	Rare	Abundant	Common	Common	Abundant	Rare	Common	Abundant
74.07	SN-8	Abundant	Abundant	Common	Rare	Rare	Abundant	Common	Common	Abundant	Common	Common	Abundant
83.02	SN-39	Abundant	Abundant	Common	Common	Common	Abundant	Common	Common	Abundant	Common	Common	Abundant
87.98	SN-9	Abundant	Abundant	Common	Rare	Rare	Abundant	Common	Common	Abundant	Common	Common	Abundant
92.82	SN-41	Abundant	Abundant	Common	Rare	Rare	Abundant	Common	Common	Abundant	Common	Common	Common
98.25	SN-10	Abundant	Abundant	Common	Rare	Rare	Abundant	Common	Common	Abundant	Rare	Abundant	Abundant
111.10	SN-11	Abundant	Abundant	Common	Rare	Rare	Abundant	Common	Common	Abundant	Common	Common	Abundant
117.13	SN-40	Abundant	Abundant	Common	Rare	Rare	Abundant	Common	Common	Abundant	Common	Common	Common
176.50	SN-12	Abundant	Abundant	Common	Rare	Rare	Abundant	Common	Common	Abundant	Common	Common	Common
182.62	SN-42	Abundant	Abundant	Common	Rare	Rare	Abundant	Common	Common	Abundant	Common	Common	Abundant
226.70	SN-13	Abundant	Abundant	Common	Rare	Rare	Abundant	Common	Common	Abundant	Common	Common	Abundant
285.51	SN-43	Abundant	Abundant	Common	Rare	Rare	Abundant	Common	Common	Abundant	Common	Common	Common
369.19	SN-14	Abundant	Abundant	Common	Rare	Rare	Abundant	Common	Common	Abundant	Common	Common	Common
394.01	SN-44	Abundant	Abundant	Common	Rare	Rare	Abundant	Common	Common	Abundant	Common	Common	Abundant
426.68	SN-15	Abundant	Abundant	Common	Rare	Rare	Abundant	Common	Common	Abundant	Common	Common	Common
486.72	SN-45	Abundant	Abundant	Common	Rare	Rare	Abundant	Common	Common	Abundant	Common	Common	Common
505.32	SN-16	Abundant	Abundant	Common	Rare	Rare	Abundant	Common	Common	Abundant	Common	Common	Common
592.42	SN-17	Abundant	Abundant	Common	Rare	Rare	Abundant	Common	Common	Abundant	Common	Common	Common
621.2	SN-46	Abundant	Abundant	Common	Rare	Rare	Abundant	Common	Common	Abundant	Common	Common	Common
630.55	SN-18	Abundant	Abundant	Common	Rare	Rare	Abundant	Common	Common	Abundant	Common	Common	Common
737.39	SN-19	Abundant	Abundant	Common	Rare	Rare	Abundant	Common	Common	Abundant	Common	Common	Common
737.47	SN-47	Abundant	Abundant	Common	Rare	Rare	Abundant	Common	Common	Abundant	Common	Common	Common
751.16	SN-20	Abundant	Abundant	Common	Rare	Rare	Abundant	Common	Common	Abundant	Common	Common	Rare



Table 2: Continued

Depth (mbsf)	Sample no	Clay domain pores				Silt adjacent pores								
		Small pores (<5x10 <sup>5</sup> nm <sup>2</sup> )	Larger pores (>5x10 <sup>5</sup> nm <sup>2</sup> )	Small pore	Larger pore	Elongate linear	Elongate crescent	Equant	Elongate linear	Elongate crescent	Equant			
776.17	SN-21	Abundant	Rare	Abundant	Rare	Rare	Rare	Common	Common	Abundant	Common	Abundant	Common	Rare
802.55	SN-22	Abundant	Rare	Abundant	Rare	Rare	Rare	Common	Common	Abundant	Common	Abundant	Common	Common
841.56	SN-48	Abundant	Rare	Abundant	Rare	Rare	Rare	Common	Common	Abundant	Rare	Abundant	Common	Rare
871.87	SN-23	Abundant	Rare	Abundant	Rare	Rare	Rare	Common	Common	Abundant	Common	Common	Common	Common
929.81	SN-24	Abundant	Rare	Abundant	Rare	Rare	Rare	Common	Common	Abundant	Common	Common	Common	Rare
959.15	SN-49	Abundant	Rare	Abundant	Rare	Rare	Rare	Common	Common	Abundant	Rare	Common	Common	Common
971.26	SN-25	Abundant	Rare	Abundant	Rare	Rare	Rare	Common	Common	Abundant	Rare	Abundant	Common	Common
1026.3	SN-50	Abundant	Rare	Abundant	Rare	Rare	Rare	Common	Common	Abundant	Common	Common	Common	Common
1027.9	SN-26	Abundant	Rare	Abundant	Rare	Rare	Rare	Common	Common	Abundant	Common	Abundant	Common	Common
1095.7	SN-27	Abundant	Rare	Abundant	Rare	Rare	Rare	Common	Common	Abundant	Common	Common	Common	Rare
1119.7	SN-28	Abundant	Rare	Abundant	Rare	Rare	Rare	Common	Rare	Abundant	Common	Common	Common	Common
1145.9	SN-51	Abundant	Rare	Abundant	Rare	Rare	Rare	Common	Common	Abundant	Common	Common	Rare	Rare
1172.8	SN-29	Abundant	Rare	Abundant	Rare	Rare	Rare	Abundant	Abundant	Abundant	Common	Rare	Common	Abundant
1184.3	SN-30	Abundant	Rare	Abundant	Rare	Rare	Rare	Common	Common	Abundant	Common	Common	Common	Rare
1233.1	SN-31	Abundant	Rare	Abundant	Rare	Rare	Rare	Common	Rare	Abundant	Common	Common	Common	Common
1251.5	SN-52	Abundant	Rare	Abundant	Rare	Rare	Rare	Common	Rare	Abundant	Rare	Common	Common	Rare
1267.1	SN-32	Abundant	Rare	Abundant	Rare	Rare	Rare	Common	Common	Abundant	Common	Common	Rare	Rare
1299.3	SN-33	Abundant	Rare	Abundant	Rare	Rare	Rare	Common	Rare	Abundant	Common	Common	Rare	Rare
1358.9	SN-53	Abundant	Rare	Abundant	Rare	Rare	Rare	Common	Common	Abundant	Common	Common	Common	Common
1432.5	SN-54	Abundant	Rare	Abundant	Rare	Rare	Rare	Common	Rare	Abundant	Rare	Common	Common	Rare



Table 3: Micromechanical particle deformation process with depth

Depth	Sample	EE	EF	FF	Elongate particle bending	Cross particle fracture
1.24	SN-1	Rare	Abundant	Common	Rare	Absent
5.10	SN-2	Rare	Abundant	Common	Rare	Absent
6.25	SN-34	Rare	Common	Abundant	Rare	Absent
7.21	SN-35	Rare	Common	Abundant	Rare	Absent
9.18	SN-3	Rare	Common	Abundant	Rare	Absent
10.69	SN-4	Rare	Common	Abundant	Rare	Absent
14.28	SN-36	Rare	Common	Abundant	Rare	Absent
26.05	SN-5	Rare	Common	Abundant	Rare	Absent
28.00	SN-6	Rare	Rare	Abundant	Rare	Absent
28.12	SN-37	Rare	Common	Abundant	Rare	Rare
50.82	SN-38	Rare	Rare	Abundant	Rare	Absent
63.24	SN-7	Rare	Rare	Abundant	Rare	Absent
74.07	SN-8	Rare	Rare	Abundant	Rare	Absent
83.02	SN-39	Rare	Rare	Abundant	Rare	Absent
87.98	SN-9	Rare	Rare	Abundant	Rare	Absent
92.82	SN-41	Rare	Rare	Abundant	Rare	Absent
98.25	SN-10	Rare	Common	Abundant	Common	Absent
111.10	SN-11	Rare	Rare	Abundant	Common	Rare
117.13	SN-40	Rare	Rare	Abundant	Rare	Absent
176.50	SN-12	Rare	Rare	Abundant	Rare	Absent
182.62	SN-42	Rare	Rare	Abundant	Common	Absent
226.70	SN-13	Rare	Rare	Abundant	Common	Absent
285.51	SN-43	Rare	Rare	Abundant	Rare	Absent
369.19	SN-14	Rare	Rare	Abundant	Common	Absent
394.01	SN-44	Rare	Rare	Abundant	Common	Absent
426.68	SN-15	Rare	Rare	Abundant	Common	Absent
486.72	SN-45	Rare	Rare	Abundant	Rare	Absent
505.32	SN-16	Rare	Rare	Abundant	Common	Absent
592.42	SN-17	Rare	Rare	Abundant	Common	Absent
621.2	SN-46	Rare	Rare	Abundant	Rare	Absent
630.55	SN-18	Rare	Common	Abundant	Common	Rare
737.39	SN-19	Rare	Rare	Abundant	Rare	Rare
737.47	SN-47	Rare	Rare	Abundant	Rare	Absent
751.16	SN-20	Rare	Rare	Abundant	Common	Absent
776.17	SN-21	Rare	Rare	Abundant	Common	Absent
802.55	SN-22	Rare	Rare	Abundant	Rare	Absent
841.56	SN-48	Rare	Rare	Abundant	Common	Absent
871.87	SN-23	Rare	Rare	Abundant	Common	Rare
929.81	SN-24	Rare	Rare	Abundant	Rare	Rare
959.15	SN-49	Rare	Rare	Abundant	Rare	Rare
971.26	SN-25	Rare	Rare	Abundant	Common	Rare
1026.3	SN-50	Rare	Rare	Abundant	Common	Absent
1027.9	SN-26	Rare	Rare	Abundant	Common	Absent
1095.7	SN-27	Rare	Rare	Abundant	Common	Absent
1119.7	SN-28	Rare	Rare	Abundant	Common	Rare
1145.9	SN-51	Rare	Rare	Abundant	Rare	Absent
1172.8	SN-29	Rare	Rare	Abundant	Common	Rare
1184.3	SN-30	Rare	Rare	Abundant	Common	Absent
1233.1	SN-31	Rare	Rare	Abundant	Common	Rare
1251.5	SN-52	Rare	Rare	Abundant	Rare	Absent
1267.1	SN-32	Rare	Rare	Abundant	Abundant	Rare
1299.3	SN-33	Rare	Rare	Abundant	Abundant	Absent
1358.9	SN-53	Rare	Rare	Abundant	Common	Absent
1432.5	SN-54	Rare	Rare	Abundant	Common	Absent